

Decrease in tropospheric O₃ levels of the Northern Hemisphere observed by IASI

Catherine Wespes¹, Daniel Hurtmans¹, Cathy Clerbaux^{1,2}, Anne Boynard² and Pierre-François Coheur¹

¹Spectroscopie de l'Atmosphère, Service de Chimie Quantique et Photophysique, Faculté des Sciences, Université Libre de Bruxelles (ULB), Bruxelles, Belgique

²LATMOS/IPSL, UPMC Univ. Paris 06 Sorbonne Universités, UVSQ, CNRS, Paris, France

Abstract

In this study, we describe the recent changes in the tropospheric ozone (O₃) columns measured by the Infrared Atmospheric Sounding Interferometer (IASI) onboard the Metop satellite during the first 9 years of the IASI operation (January 2008 to May 2017). Using appropriate multivariate regression methods, we discriminate significant linear trends from other sources of O₃ variations captured by IASI. The geographical patterns of the adjusted O₃ trends are provided and discussed on the global scale. Given the large contribution of the natural variability in comparison with that of the trend (25-85% vs 15- 50%, respectively) to the total O₃ variations, we estimate that additional years of IASI measurements are generally required to detect the estimated O₃ trends with a high precision. Globally, additional 6 months to 6 years of measurements, depending on the regions and the seasons, are needed to detect a trend of |5| DU/decade. An exception is interestingly found during summer at mid-high latitudes of the North Hemisphere (N.H.; ~ 40°N-75°N) where the large absolute fitted trend values (~|0.5| DU/yr on average) combined with the small model residuals (~10%) allow the detection of a band-like pattern of significant negative trends. This finding is consistent with the reported decrease in O₃ precursor emissions in recent years, especially in Europe and US. The influence of continental pollution on that latitudinal band is further investigated and supported by the analysis of the O₃-CO relationship (in terms of correlation coefficient, regression slope and covariance) that we found to be the strongest at northern mid-latitudes in summer.

1 Introduction

O₃ plays a key role throughout the whole troposphere where it is produced by the photochemical oxidation of carbon monoxide (CO), non-methane volatile organic compounds (NMVOCs) and methane (CH₄) in the presence of nitrogen oxides (NO_x) (e.g. Logan et al., 1981). O₃ sources in the troposphere are the in situ photochemical production from anthropogenic and natural precursors, and the downwards transport of stratospheric O₃. Being a strong pollutant, a major reactive species and an important greenhouse gas in the upper troposphere, O₃ is of highest interest for air quality, atmospheric chemistry and radiative forcing studies. Thanks to its long lifetime (several weeks) relatively to transport timescales in the free troposphere (Fusco and Logan, 2003),

40 O₃ also contributes to large-scale transport of pollution far from source regions with further
41 impacts on global air quality (e.g. Stohl et al., 2002; Parrish et al., 2012) and climate. Monitoring
42 and understanding the time evolution of tropospheric O₃ at a global scale is, therefore, crucial to
43 apprehend future climate changes. Nevertheless, a series of limitations make O₃ trends particularly
44 challenging to retrieve and to interpret.

45

46 Since the 1980s, while the O₃ precursors anthropogenic emissions have increased and shifted
47 equatorward in the developing countries (Zhang et al., 2016), extensive campaigns and routine in
48 situ and remote measurements at specific urban and rural sites have provided long-term but sparse
49 datasets of tropospheric O₃ (e.g. Cooper et al., 2014 and references therein). Ultraviolet and Visible
50 (UV/VIS) atmospheric sounders onboard satellites provide tropospheric O₃ measurements with a
51 much wider coverage, but they result either from indirect methods (e.g. Fishman et al., 2005) or
52 from direct retrievals which are limited by coarse vertical resolution (Liu et al., 2010). All these
53 datasets also suffer from a lack of homogeneity in terms of measurement methods (instrument and
54 algorithm) and spatio-temporal samplings (e.g. Doughty et al., 2011). Those limitations, in
55 addition to the large natural inter-annual variability (IAV) and decadal variations in tropospheric
56 O₃ levels (due to large-scale dynamical modes of O₃ variations and to changes in stratospheric O₃,
57 in stratosphere-troposphere exchanges, in precursor emissions and in their geographical patterns),
58 introduce strong biases in trends determined from independent studies and datasets (e.g. Zbinden
59 et al., 2006; Thouret et al., 2006; Logan et al., 2012 ; Parrish et al., 2012 and references therein).
60 As a consequence, determining accurate trends requires a long period of high density and
61 homogeneous measurements (e.g. Payne et al., 2017).

62

63 Such long-term datasets are now becoming obtainable with the new generation of nadir-looking
64 and polar-orbiting instruments measuring in the thermal infrared region. In particular, about one
65 decade of O₃ profile measurements, with a good sensitivity in the troposphere independently from
66 the layers above, is now available from the IASI (Infrared Atmospheric Sounding Interferometer)
67 sounder aboard the European Metop platforms, allowing to monitor regional and global variations
68 in tropospheric O₃ levels (e.g. Dufour et al., 2012; Safieddine et al., 2013; Wespes et al., 2016).

69

70 In this study, we examine the tropospheric O₃ changes behind the natural IAV as measured by
71 IASI over January 2008-May 2017. To that end, we use the approach described in Wespes et al.
72 (2017), which relies on a multi-linear regression (MLR) procedure, for accurately differentiating
73 trends from other sources of O₃ variations; the latter being robustly identified and quantified in
74 that companion study. In Section 2, we briefly review the IASI mission and the tropospheric O₃
75 product, and we shortly describe the multivariate models (annual or seasonal) that we use for fitting
76 the daily O₃ time series. In Section 3, after verifying the performance of the MLR models over the
77 available IASI dataset, we evaluate the feasibility to capture and retrieve significant trend
78 parameters, apart from natural O₃ dependencies, by performing trend sensitivity studies. In Section
79 4, we present and discuss the global distributions of the O₃ trends estimated from IASI in the

80 troposphere. The focus is given in summer over and downwind anthropogenic polluted areas of
81 the N.H. where the possibility to infer significant trends from the first ~9 years of available IASI
82 measurements is demonstrated. Finally, the O₃-CO correlations, enhancement ratios and
83 covariance are examined for characterizing the origin of the air masses in regions of positive and
84 negative trends.

85

86 **2 IASI O₃ measurements and multivariate regression**

87

88 The IASI instrument is a nadir-viewing Fourier transform spectrometer that records the thermal
89 infrared emission of the Earth-atmosphere system between 645 and 2760 cm⁻¹ from the polar Sun-
90 synchronous orbiting meteorological Metop series of satellites. Metop-A and -B have been
91 successively launched in October 2006 and September 2012. The third and last launch is planned
92 in 2018 with Metop-C to ensure homogeneous long-term IASI measurements. The measurements
93 are taken every 50 km along the track of the satellite at nadir and over a swath of 2200 km across
94 track, with a field of view of four simultaneous footprints of 12 km at nadir, which provides global
95 coverage of the Earth twice a day (at 9:30 AM and PM mean local solar time). The instrument
96 presents a good spectral resolution and a low radiometric noise, which allows the retrieval of
97 numerous gas-phase species in the troposphere (e.g. Clerbaux et al., 2009, and references therein;
98 Hilton et al., 2012; Clarisse et al., 2011).

99

100 In this paper, we use the FORLI-O₃ profiles (Fast Optimal Retrievals on Layers for IASI
101 processing chain set up at ULB; v20151001) retrieved from the IASI-A (aboard Metop-A) daytime
102 measurements (defined with a solar zenith angle to the sun < 80°) which are characterized by a
103 good spectral fit (determined here by quality flags on biased or sloped residuals, suspect averaging
104 kernels, maximum number of iteration exceeded,...) and which correspond to clear or almost-clear
105 scenes (a filter based on a fractional cloud cover below 13% has been applied; cfr Clerbaux et al.,
106 2009; Hurtmans et al., 2012). These profiles are characterized by a good vertical sensitivity in the
107 troposphere and the stratosphere (e.g. Wespes et al., 2017). The FORLI algorithm relies on a fast
108 radiative transfer and retrieval methodology based on the Optimal Estimation Method (Rodgers,
109 2000) and is fully described in Hurtmans et al. (2012). The FORLI-O₃ profiles, which are retrieved
110 at 40 constant vertical layers from surface up to 40 km and an additional 40-60 km one, have
111 already undergone thorough characterization and validation exercises (e.g. Anton et al., 2011;
112 Dufour et al., 2012; Gazeaux et al., 2012; Hurtmans et al., 2012; Parrington et al., 2012; Pommier
113 et al., 2012; Scannell et al., 2012; Oetjen et al., 2014; Boynard et al., 2016; Wespes et al., 2016;
114 Keppens et al. 2017; Boynard et al., 2017). They demonstrated a good degree of accuracy, of
115 precision and of vertical sensitivity with no instrumental drift, to capture the large-scale dynamical
116 modes of O₃ variability in the troposphere independently from the layers above (Wespes et al.,
117 2017), with the possibility to further differentiate long-term O₃ changes in the troposphere (Wespes
118 et al., 2016). Note, however, that a drift in the N.H. MLT O₃ over the whole IASI dataset is reported
119 in Keppens et al. (this issue) and Boynard et al. (this issue) from comparison with O₃ sondes. This

120 drift (~2.8DU/dec in the N.H.) is shown in Boynard et al. (this issue) to result from a discontinuity
121 (“jump” as called in Boynard et al., this issue) in September 2010 in the IASI O₃ time series, for
122 reasons that are unclear at present. Furthermore, the drift strongly decreases (<|1| DU/dec on
123 average) after the “jump” and it becomes even non-significant for most of the stations (significant
124 positive drift is also found for some stations) over the periods before or after the jump, separately.
125

126 For the purpose of this work, we focus on a tropospheric column ranging from ground to 300 hPa
127 (called MLT – Middle-Low Troposphere – in this study) that includes the altitude of maximum
128 sensitivity of IASI in the troposphere (usually between 4 and 8 km altitude), which limits as much
129 as possible the influences of the stratospheric O₃ and that was shown in Wespes et al. (2017) to
130 exhibit independent deseasonalized anomalies/dynamical processes from those in the stratospheric
131 layers. The stratospheric contribution into the tropospheric O₃ columns have been previously
132 estimated in Wespes et al. (2016) as ranging between 30% and 65% depending on the region and
133 the season with the smallest contribution as well as the largest sensitivity in the northern mid-
134 latitudes in spring-summer where the O₃ variations, hence, mainly originate from the troposphere.
135 We use almost the same MLR model (in its annual or its seasonal formulation) as the one
136 developed in the companion paper (see Eq.1 and 2; Section 2.2 in Wespes et al., 2017), which
137 includes a series of geophysical variables in addition to a linear trend (LT) term. In order to take
138 account of the observed “jump” properly, we modified the previously used MLR model so that the
139 constant term is split into two components covering the periods before and after the September
140 2010 “jump”, separately. The MLR which is performed using an iterative stepwise backward
141 elimination approach to retain the most relevant explanatory variables (called “proxies”) at the end
142 of the iterations (e.g. Mäder et al., 2007) is applied on the daily IASI O₃ time series. The main
143 selected proxies used to account for the natural variations in O₃ are namely the QBO (Quasi-
144 Biennial Oscillation), the NAO (North Atlantic Oscillation) and the ENSO (El Niño–Southern
145 Oscillation) (cfr Table 1 in Wespes et al. (2017) for the exhaustive list of the used proxies). Their
146 associated standard errors are estimated from the covariance matrix of the regression coefficients
147 and are corrected to take into account the uncertainty due to the autocorrelation of the noise
148 residual (see Eq. 3 in Wespes et al. (2016)). The common rule that the regression coefficients are
149 significant if they are greater in magnitude than 2 times their standard errors is applied (95%
150 confidence limits defined by 2σ level). The MLR model was found to give a good representation
151 of the IASI O₃ records in the troposphere over 2008-2016, allowing us to identify/quantify the
152 main O₃ drivers with marked regional differences in the regression coefficients. Time-lags of 2
153 and 4 months for ENSO are also included hereafter in the MLR model to account for a large but
154 delayed impact of ENSO on mid- and high latitudes O₃ variations far from the Equatorial Pacific
155 where the ENSO signal originates (Wespes et al., 2017).

156

157 **3 Regression performance and sensitivity to trend**

158

159 In this section, we first verify the performance of the MLR models (annual and seasonal; in terms
160 of residual errors and variation explained by the model) to globally reproduce the time evolution
161 of O₃ records over the entire studied period (January 2008 – May 2017). Based on this, we then
162 investigate the statistical relevance for a trend study from IASI in the troposphere by examining
163 the sensitivity of the pair IASI-MLR to the retrieved LT term.
164

165 Figure 1 presents the seasonal distributions of tropospheric O₃ measured by IASI averaged over
166 January 2008 – May 2017 (left panels), along with the root-mean-squared error of the seasonal
167 regression fit (*RMSE*, in DU; middle panels) and the contribution of the fitted seasonal model into

168 the IASI O₃ time series (in %; right panels), calculated as $\frac{\sigma(O_3^{\text{Fitted_model}}(t))}{\sigma(O_3(t))}$ where σ is the standard

169 deviation relative to the regression models and to the IASI O₃ time series. These two statistical
170 parameters help to evaluate how well the fitted model explains the variability in the IASI O₃
171 observations. The seasonal patterns of O₃ measurements are close to those reported in Wespes et
172 al. (2017) for a shorter period (see Section 2.1 and 3.1 in Wespes et al. (2017) for a detailed
173 description of the distributions) and they clearly show, for instance, high O₃ values over the highly
174 populated areas of Asia in summer. The distributions from Fig.1 show that the model reproduces
175 between 35% and 90% of the daily O₃ variation captured by IASI and that the residual errors varies
176 between 0.01 DU and 5 DU (i.e. the *RMSE* relative to the IASI O₃ time series are of ~15% on
177 global average and vary between 10% in the N.H. in summer and 30% in specific tropical regions).
178 On an annual basis (data not shown), the model explains a large fraction of the variation in the
179 IASI O₃ dataset (from ~45% to ~85%) and the *RMSE* are lower than 4.5 DU everywhere (~3 DU
180 on the global average). The relative *RMSE* is less than 1% in almost all situations indicating the
181 absence of bias.
182

183 The seasonal distributions of the contribution to the total variation in the MLT from the adjusted
184 harmonic terms and explanatory variables, which account for the “natural” variability, and from
185 the LT term are shown in Fig. 2 (left and right panels, respectively). The grey areas in the LT
186 panels refer to the LT terms rejected by the stepwise backward elimination process. The crosses
187 indicate that the trend estimate in the grid cell is non-significant in the 95% confidence limits (2 σ
188 level) when accounting for the autocorrelation in the noise residual at the end of the elimination
189 procedure. While the large influence of the seasonal variations and of the main drivers - namely
190 ENSO, NAO and QBO - on the IASI O₃ records has been clearly attested in Wespes et al. (2017),
191 we demonstrate in Fig.2 that the LT also contributes considerably to the O₃ variations detected by
192 IASI in the troposphere. The LT contribution generally ranges from 15% to 50%, with the largest
193 values (~30-50%) being observed at mid-high latitudes in the S.H. (30°S-70°S) and in the N.H.
194 (~45°N-70°N) in summer. In the S.H., they are associated with the smallest tropospheric O₃
195 columns (Fig.1; left panels) and the smallest natural contributions (<25%; left panels), while in the
196 N.H. summer, they interestingly correspond to large MLT O₃ columns, large natural contributions

197 (~50-60%) and the smallest *RMSE* (<12 % or <3 DU). From the annual regression model, the
198 natural variation and the trend contribute respectively for 30-85% and up to 40% to the total
199 variation in the MLT.

200 In Fig.3, we further investigate the robustness of the estimated trends by performing sensitivity
201 tests in regions of significant trend contributions (e.g. in the N.H. mid-latitudes in summer; cfr
202 Fig.2). The ~9-year time series of IASI O₃ daily averages (dark blue) along with the results from
203 the seasonal regression model with and without the LT term included in the model (light blue and
204 orange lines, respectively) are represented in the top row panel for one specific location (Fig.3a
205 and b; highlighted by a blue circle in the JJA panel in Fig.4). The second row panel provides the
206 deseasonalised IASI (dark blue line) and fitted time series (calculated by subtracting the adjusted
207 seasonal cycle from the time series) resulting from the adjustment with and without the LT term
208 included in the MLR model (light blue and orange lines, respectively). The differences between
209 the fitted models with and without LT are shown in the third rows (pink lines). They match fairly
210 well the adjusted trend over the IASI period (3^d row panel, grey lines; the trend and the *RMSE*
211 values are also indicated) and the adjustment without LT leads to larger residuals (e.g.
212 *RMSE*_{JJA_wo_LT}=3.37 DU vs. *RMSE*_{JJA_with_LT}=3.21 DU in summer). This result demonstrates the
213 possibility to capture trend information from ~9 years of IASI-MLR with only some compensation
214 effects by the other explanatory variables, contrary to what was observed when considering a
215 shorter period of measurements or a lesser temporal sampling (i.e. monthly dataset; e.g. Wespes
216 et al., 2016). It is also worth to mention that the O₃ changes calculated over the whole IASI dataset
217 in summer are larger than the *RMSE* of the model residuals (increase of 5.39±1.86 DU vs *RMSE*
218 of 3.21 DU), underlying the statistical relevance of trend estimates.

219 The robustness of the adjusted trend is verified at the global scale in Fig.4 which represents the
220 seasonal distributions of the relative differences in the *RMSE* with and without the LT included in
221 the MLR model, calculated as $[(RMSE_{wo_LT} - RMSE_{with_LT})/RMSE_{with_LT} \times 100]$ (in %). An
222 increase in the *RMSE* when excluding LT from the MLR is observed almost everywhere in regions
223 of significant trend contributions (Fig.2), especially in mid-high latitudes of the S.H. and of the
224 N.H. in summer where it reaches 10%. This result indicates that adjusting LT improves the
225 performance of the model and, hence, that a trend signal is well captured by IASI at a regional
226 scale in the troposphere. From the annual model, the increase in the *RMSE* only reaches 5% at
227 mid-high latitudes of the S.H. (data not shown). In regions of weak or non-significant trend
228 contribution (see crosses in Fig.2), no improvement is logically found.

229

230 **4 O₃ trend over 2008-2017**

231 **4.1 Annual and seasonal trends**

232

233 The annual and the seasonal distributions of the fitted LT terms which are retained in the annual
234 and the seasonal MLR models by the stepwise elimination procedure are respectively represented

235 in Fig. 5 (a) and (b) (in DU/yr). Generally, the mid-high latitudes of both hemispheres and, more
236 particularly, the N.H. mid-latitudes in summer reveal significant negative trends, while the tropics
237 are mainly characterized by non-significant or weak significant trends. Even if trends in emissions
238 have already been able to qualitatively explain measured tropospheric O₃ trends over specific
239 regions, the magnitude and the trend estimates considerably vary between independent
240 measurement datasets (e.g. Cooper et al., 2014; the TOAR report – Tropospheric Ozone
241 Assessment Report: Present-day distribution and trends of tropospheric ozone relevant to climate
242 and global atmospheric chemistry model evaluation, Lead Authors: A. Gaudel and O.R. Cooper –
243 coordinated by the International Global Atmospheric Chemistry Project and available on
244 <http://www.igacproject.org/activities/TOAR> and submitted to Elementa; and references therein)
245 for the reasons discussed in Section 1 and they are not reproduced/explained by model simulations
246 (e.g. Jonson et al., 2006; Cooper et al., 2010; Logan et al., 2012; Wilson et al., 2012; Hess et al.,
247 2013; and references therein). As a result, comparing/reconciling the adjusted trends with
248 independent measurements, even on a qualitative basis, remains difficult. Nevertheless, several of
249 the statistically significant features observed in Fig.5 show, interestingly, qualitative consistency
250 with respect to recent published findings:

251

- 252 - The S.H. tropical region extending from the Amazon to tropical eastern Indian Ocean
253 seems to indicate a general increase with, for example, a DJF trend of $\sim 0.23 \pm 0.18$ DU/yr
254 (i.e. 2.09 ± 1.70 DU over the IASI measurement period), despite the large IAV in the MLT
255 which characterizes the tropics and which likely explains the high frequency of non-
256 significant trends. Enhanced O₃ levels over that region have already been analysed for
257 previous periods (e.g. Logan et al., 1985, 1986; Fishman et al., 1991; Moxim et al., 2000;
258 Thompson et al., 2000, 2007; Sauvage et al., 2006, 2007; Archibald et al., 2017). For
259 instance, the large O₃ enhancement of $\sim 0.36 \pm 0.25$ DU/yr (i.e. 3.3 ± 2.3 DU over the whole
260 IASI period) stretching from southern Africa to Australia over the north-east of
261 Madagascar during the austral winter-spring likely originates from large IAV in the
262 subtropical jet-related stratosphere–troposphere exchanges which have been found to
263 primarily contribute to the tropospheric O₃ trends over that region (Liu et al., 2016; 2017).
264 Nevertheless, this finding should be mitigated by the fact that the trend value in the S.H.
265 tropics is of the same magnitude as the *RMSE* of the regression residuals (~ 2 -4.5 DU; see
266 Fig.1).

267

- 268 - The trends over the South-East Asia are mostly non-significant and vary by season. In
269 spring-summer, some grid cells in India, in mainland China and eastwards downwind
270 China exhibit significant positive trends reaching ~ 0.45 DU/yr (i.e. ~ 4.2 DU over the IASI
271 measurement period). This tends to indicate that the tropospheric O₃ increases which have
272 been shown to mainly result from a strong positive trend in the Asian emissions over the
273 past decades (e.g. Zhao et al., 2013; Cooper et al., 2014; Zhang et al., 2016; Cohen et al.,
274 2017; Tarasick et al., 2017; and references therein) but also from a substantial change in

275 the stratospheric contribution (Verstraeten et al., 2015) persists through 2008-2017 despite
276 the recent decrease in O₃ precursor emissions recorded in China after 2011 (e.g. Duncan et
277 al., 2016; Krotkov et al., 2016; Miyazaki et al., 2017; Van der A et al. 2017). This would
278 indicate that this decrease is probably too recent/weak to recover the 2008 O₃ levels over
279 the entire region. Note, however, that this finding has to be taken carefully given the large
280 model residuals (*RMSE* of ~2-4 DU; cfr Section 3, Fig.1) over that region. Finally, the large
281 uncertainty in trend estimates over the South-East Asia might reflect the large IAV in the
282 biomass-burning emissions and lightning NO_x sources, in addition to the recent changes in
283 emissions.

284
285 - The mid- and high latitudes of the S.H. show clear patterns of negative trends, all over the
286 year and in a more pronounced manner during winter-spring, with larger amplitudes than
287 those of the *RMSE* values (~-0.33±0.14 DU/yr on average in the 35°S-65°S band; i.e. a
288 trend amplitude of ~|3.1|±1.3 DU over the studied period vs a *RMSE* value of ~2.5 DU).
289 These significant negative trends in the S.H. are hard to explain but, considering the
290 stratospheric contribution into the tropospheric columns (natural and artificial due to the
291 limited IASI vertical sensitivity) in the mid-high latitudes of the S.H. (~40-60%; see
292 supplementary materials in Wespes et al., 2016) and the negative significant trends
293 previously reported from IASI in the UTLS/low stratosphere in the 30°S-50°S band, they
294 could be in line with those derived by Zeng et al. (2017) in the UTLS for a clean rural site
295 of the S.H. (Lauder, New Zealand), which mainly originate from increasing tropopause
296 height and O₃ depleting substances.

297
298 - In the N.H., a band-like pattern of negative trends is observed in the 40°N-75°N latitudes
299 covering Europe and North America, especially during summer. Averaged annual trend of
300 -0.31±0.17 DU/yr and summer trend of -0.47±0.22 DU/yr (i.e. -2.87±1.57 DU and -
301 4.36±2.02 DU, respectively, from January 2008 to May 2017) are estimated in that
302 latitudinal band. These trend values are significantly larger than the *RMSE* of the MLR
303 model (<3.5 DU in JJA; cfr Section 3, Fig.1). Interestingly, both the annual and summer
304 trends are amplified relative to the ones calculated in the mid-latitudes of the N.H. over the
305 2008-2013 period of IASI measurements (-0.19±0.05 DU/yr and -0.30±0.10 DU/yr for the
306 annual and the summer trends, respectively, calculated in the 30°N-50°N band; see Wespes
307 et al. (2016)). This finding is line with previous studies which point out a possible leveling
308 off of tropospheric O₃ in summer due to the decline of anthropogenic O₃ precursor
309 emissions observed since 2010-2011 in North America, in Western Europe and also in
310 some regions of China (e.g. Cooper et al., 2010; 2012; Logan et al., 2012; Parrish et al.,
311 2012; Oltmans et al., 2013; Simon et al., 2015; Archibald et al., 2017; Miyazaki et al.,
312 2017). It even goes a step further by suggesting a possible decrease in the tropospheric O₃
313 levels. Archibald et al. (2017) recently reported a net decrease of ~5% in the global
314 anthropogenic NO_x emissions in the 30°N-90°N latitude band, which is consistent with the

315 annual significant negative trend of -0.27 ± 0.15 DU/yr for O₃ estimated from IASI in that
 316 band. We should also note that, even if these latitudes are characterized by the lowest
 317 stratospheric contribution (~30-45%; see supplementary materials in Wespes et al., 2016),
 318 it might partly mask/attenuate the variability in the tropospheric O₃ levels.

319

320 4.2 Expected year for trend detection

321

322 In this section, we further verify that it is indeed possible to infer, from the studied IASI period,
 323 the significant negative trend derived in the 40°N-75°N band in summer ($\sim|0.5|$ DU/yr on average,
 324 see Section 4.1) by determining the expected year from which such a trend amplitude would be
 325 detectable at a global scale. This is achieved by estimating the minimum duration (with probability
 326 0.90) of the IASI O₃ measurements that would be required to detect a trend of a specified
 327 magnitude, and its 95% confidence level, following the formalism developed in Tiao et al. (1990)
 328 and in Weatherhead et al. (1998):

$$329 \quad N^* \approx \left[\frac{3.3 \cdot \sigma_\varepsilon}{|\tau_{yr}|} \cdot \sqrt{\frac{1+\Phi}{1-\Phi}} \right]^{2/3} \quad \text{Eq (1)}$$

$$330 \quad CL_{N^*} = [N^* \cdot e^{-B}; N^* \cdot e^{+B}] \quad \text{Eq (2)}$$

331 Where N^* is the number of the required years, σ_ε is the standard deviation of the autoregressive
 332 noise residual ε_t , τ_{yr} is the magnitude of the trend per year, Φ is the lag-1 autocorrelation of the
 333 noise. The magnitude of the variation and of the autocorrelation in the noise residuals are taken
 334 into account for a better precision on the trend estimate. Given that large variance (σ_ε^2) and large
 335 positive autocorrelation Φ of the noise induce small signal-to-noise ratio and long trend-like
 336 segments in the dataset, respectively, these two parameters increase the number of years that would
 337 be required for detecting a specified trend. CL_{N^*} is the 95% confidence limits which is not
 338 symmetric around N^* and depends on B , an estimated uncertainty factor calculated as

$$339 \quad \frac{4}{3\sqrt{D}} \sqrt{\frac{1+\Phi}{1-\Phi}}, \text{ with } D \text{ the number of days in the IASI datasets, which accounts for the uncertainty}$$

340 in Φ (the uncertainty in σ_ε being negligible given that only a few years of data are needed to
 341 estimate it; cfr Weatherhead et al. (1998)). As a result, based on the available IASI-A and proxies
 342 datasets and assuming that the MLR model used in this study is accurate, we estimate, in Fig. 6 (a)
 343 and (b), the expected year when an O₃ trend amplitude of $|5|$ DU per decade (i.e. $\tau_{yr} = |0.5|$ DU/yr
 344 which corresponds to the averaged absolute value of the fitted negative trends in the N.H. summer;
 345 see Fig.5b) is detectable, and its associated maximal confidence limit, respectively. The results in
 346 Fig. 6 clearly demonstrates the possibility to infer, from the available IASI dataset, such significant

347 trends in the mid- and high latitudes of the N.H. in summer and fall (trend detectable from ~2016-
348 2017 with an uncertainty of ~6-9 months; cfr Fig.6b). On the contrary, the tropical regions and the
349 N.H. in winter-spring would require additional ~ 6 months to 6 years of measurements to detect
350 an amplitude of $|0.5|$ DU/yr (trend significant only from ~ 2017 – 2023 or after depending on the
351 location and the season). Note also that the strongest negative trends (up to -0.85 DU/yr, i.e. $\tau_{yr} =$
352 $|0.85|$ DU/yr, see Fig.5b) observed in specific regions of the N.H. mid-latitudes would only require
353 ~6 years of IASI measurements for being detected. The mid- and high latitudes of the S.H. would
354 require the shortest period of IASI measurement for detecting a specified trend, with only ~7 years
355 ± 6 months of IASI measurements to detect a $|0.5|$ DU/yr trend (trend detectable from ~2015). That
356 band-like pattern in the S.H. corresponds to the region with the weakest IAV and contribution from
357 large-scale dynamical modes of variability in the IASI MLT columns (see Section 3, Fig.1 and 2),
358 which translates into small σ_ϵ^2 and Φ . Note however that an additional few months of IASI data
359 are required to confirm the smaller negative trend of ~ -0.35 DU/yr measured on average in the
360 S.H. (see Fig.5; a period ~ 9 years ± 6 months being necessary to detect a trend amplitude of $|3.5|$
361 DU/dec). Given that large σ_ϵ means large noise residual in the IASI data, the regions of short or
362 long required measurement period coincide, as expected, well with the small or high *RMSE* values
363 of the regression residuals (see Section 3, Fig. 1).

364

365 The regions of the longest measurement periods required in the tropics for a trend detection (up to
366 ~16 years of IASI data) correspond to known patterns of widespread high O_3 : (a) above intense
367 biomass burnings in Amazonia and eastwards across tropical Atlantic (Logan et al., 1986; Fishman
368 et al., 1991; Moxim et al., 2000; Thompson et al., 2000, 2007; Sauvage et al., 2007), (b) eastwards
369 Africa across the South Indian Ocean which is subject to large variations in the stratospheric
370 influences during the winter-spring austral period (JJA-SON) (Liu et al., 2016; 2017), (c)
371 Eastwards Africa across the North Indian Ocean to India likely due to large lightning NO_x
372 emissions above central Africa during the wet season associated with the northeastward jet
373 conducting a so-called “ O_3 river” (Tocquer et al., 2015) and (d) above regions of positive ENSO
374 “chemical” effect in Equatorial Asia/Australia and eastwards above northern and southern tropical
375 regions (Wespes et al., 2016) explained by reduced rainfalls and biomass fires during El Niño
376 conditions (e.g. Worden et al., 2013). In fact, most of these patterns (a, b and d) are closely
377 connected with strong El- Niño events which extend the duration of the dry season and cause
378 severe droughts, producing intense biomass burning emissions, for instance, over South America
379 (e.g. Chen et al., 2011; Lewis et al., 2011) and South Asia/Australia (e.g. Oman et al., 2013; Valks
380 et al., 2014; Ziemke et al., 2015), and which alter the tropospheric circulation by increasing the
381 transport of stratospheric O_3 into the troposphere (e.g. Voulgarakis et al., 2011; Neu et al., 2014)
382 and the transport of biomass burning air masses to the Indian Ocean (Zhang et al., 2012). In
383 summary, these large-scale indirect ENSO-related variations in tropospheric O_3 and the lightning
384 NO_x impact on O_3 , which are not accounted for in the MLR by specific representative proxies, are

385 misrepresented in the regression models. They induce large noise residuals, i.e. large σ_ϵ , and,
386 hence, extends the time period needed to detect a trend of any given magnitude.

387
388 Figure 6, finally, suggests that a long duration is also required, especially in summer, above and
389 east of China to quantify the anthropogenic impact on the local changes in the MLT: additional
390 3 ± 1.5 years or 5 ± 1.5 years for a given $|5|$ or $|3.5|$ DU/dec trend are respectively calculated. This
391 result could be explained by large perturbations in the MLT columns induced by recent decreases
392 after decades of almost constant increases in surface emissions in China (e.g. Cohen et al., 2017;
393 Miyazaki et al., 2017).

394 395 **4.3 Multi-linear vs single linear model**

396
397 Even if MLR have already been used for extracting trends in stratospheric and total O₃ columns
398 (e.g. Mäder et al., 2007; Frossard et al., 2013; Rieder et al., 2013; Knibbe et al., 2014), single linear
399 regressions (SLR) without discriminating the natural (chemical and dynamical) factors describing
400 the O₃ variability are still commonly used (e.g. Cooper et al., 2014; the TOAR report –
401 Tropospheric Ozone Assessment Report: Present-day distribution and trends of tropospheric ozone
402 relevant to climate and global atmospheric chemistry model evaluation, Lead Authors: A. Gaudel
403 and O.R. Cooper – submitted to Elementa, and references therein). They are, however, suspected
404 to contribute to trend biases retrieved between independent measurements. In addition to the time-
405 varying instrumental biases, trend biases can also be related to differences in the spatial and the
406 temporal samplings (e.g. Doughty et al., 2011; Saunio et al., 2012; Lin et al., 2015), in the
407 measurement period, in the upper boundary of the O₃ columns, in the algorithm and in the vertical
408 sensitivity of the measurements. The latter artificially alters the characteristics of the sounded layer
409 by contaminations from the above and the below layers leading to a mixing of the trend but also
410 of the natural characteristics originating from these different layers (e.g. troposphere and
411 stratosphere). The differences in the studied period, in the tropopause definition and in the spatio-
412 temporal sampling might also imply differences in the natural influence on the measured O₃
413 variations. While the impact of the natural contribution is taken into account in the MLR model, it
414 might introduce an additional bias in the trend determined from SLR, making further challenging
415 to compare trends estimated from a series of inhomogeneous independent measurements.
416 Substantial effort in homogenizing independent tropospheric O₃ column (TOCs) datasets have
417 been performed in the TOAR-climate assessment report (Gaudel et al., submitted to Elementa),
418 but large SLR trend biases remain between the TOAR datasets, in particular, between the satellite
419 datasets where the lack of homogeneity in terms of tropopause calculation (same tropopause
420 definition but different temperature profiles are used), of instrument vertical sensitivities and of
421 spatial sampling has been specifically pointed as possible causes for the trend divergence.

422

423 Reconciling the trend biases between the datasets by applying the vertical sensitivity of each
424 measurement type to a common platform, as proposed in the TOAR-climate assessment report is
425 beyond the scope of this study, but the improvement in using a MLR instead of a SLR model for
426 determining more accurate/realistic trends is explored here by comparing the seasonal distributions
427 of the trends estimated from MLR (see Fig. 5 (b) in Section 4.1.) and from SLR (presented in
428 Fig.7). Note that the constant term in the SLR is split into two components (covering the periods
429 before and after the September 2010 “jump”) to take account of the observed “jump” (see Section
430 2). The highest differences in the fitted trends derived from the two methods are found in the
431 tropics and in some regions of the mid-latitudes of the N.H. They likely result from overlaps
432 between the LT term and other covariates. For instance, the regions with high significant SLR
433 trends (~0.3-0.6 DU/yr over the tropical western and middle Pacific) during the period extending
434 from September to May match the regions with strong El Niño/Southern Oscillation influence (cfr
435 Fig. 8 and 12 in Wespes et al., 2016). On the contrary, the MLR model lends generally weak
436 significant negative or non-significant trends in the Pacific Niño region during that period and it
437 would even need additional ~3 to 4 years of IASI measurements for detecting the fitted SLR trends
438 (see Section above). The effect of ENSO in overestimating the fitted SLR trend is further illustrated
439 on Fig. 8 which represents the time series of O₃ observed by IASI and adjusted by the annual MLR
440 model (top row) along with the deseasonalized times series (middle row) and the fitted SLR and
441 MLR trends (bottom row). The fitted signal of the ENSO proxy from the MLR regression
442 (calculated as $x_j X_{norm,j}$ following Wespes et al. (2017)) is also represented (bottom row). That
443 example clearly shows that the ENSO influence is considerably compensated by the adjustment of
444 the linear trend in the SLR regression (annual trend of -0.48 ± 0.06 DU/yr from SLR vs -0.23 ± 0.16
445 DU/yr from MLR for that example). Finally, differences between the SLR and the MLR models
446 are also observed in the region with strong positive NAO influence over the Icelandic/Arctic region
447 during MAM (see Wespes et al. (2016) for a description of the NAO-related O₃ changes). On the
448 contrary, the sub-tropical S.H. exhibit similar seasonal patterns of negative trends from both the
449 SLR and the MLR. It results from the weak natural IAV and contributions in tropospheric O₃ above
450 that region (see Section 3, Fig. 1 and 2), which, hence, limits the compensation effects.

451
452 In summary, despite the fact that considering a long period of measurements is usually
453 recommended in SLR study to overcome the dynamical cycles and, hence, to help in
454 discriminating their influences from trends, we show that considering that some dynamics have
455 irregular or no particular periodicity (e.g. NAO, ENSO) it is not accurate enough. Furthermore,
456 accurate satellite measurements of tropospheric O₃ at a global scale are quite recent, limiting the
457 period of available and comparable datasets (e.g. Payne et al., 2017). As a consequence, we support
458 here that using a reliable multivariate regression model based on geophysical parameters and
459 adapted for each specific sounded layer is a robust method for differentiating a “true” trend from
460 any other sources of variability and, hence, that it should help in resolving trend differences
461 between independent datasets.

462

463 4.4 Continental influence

464

465 In this section, we use the capabilities of IASI to simultaneously measure O₃ and CO in order (1)
466 to differentiate tropospheric and stratospheric air masses, (2) to identify the regions influenced by
467 the continental export/intercontinental transport of O₃ pollution and (3) to evaluate that continental
468 influence on tropospheric O₃ trends as observed by IASI. Similar tracer correlations between CO
469 and O₃ have already been used to give insight into the photochemical O₃ enhancement in air
470 pollution transport (e.g. Parrish et al., 1993; Bertsch et al., 2005). However, there are only a few
471 studies using global satellite data for this purpose (Zhang et al., 2006; Voulgarakis et al., 2010;
472 Kim et al., 2013) and the analysis of the O₃-CO relationship for better understanding the origin of
473 O₃ trends in the troposphere has, to the best of our knowledge, never been explored.

474

475 Fig.9a and 9b show the seasonal patterns of the O₃-CO correlations (referred as R_{O₃-CO}) and of the
476 dO_3/dCO regression slopes calculated in the troposphere (from the surface to 300 hPa) over the
477 studied IASI period (January 2008 – May 2017). The dO_3/dCO regression slopes, which represent
478 the so-called O₃-CO enhancement ratio, is used to evaluate the photochemical O₃ production in
479 continental outflow regions. The R_{O₃-CO} and the dO_3/dCO distributions are similar and clearly
480 show regional and seasonal differences in the strength of the O₃-CO relationships. The patterns of
481 positive and negative correlations allows to discriminate the outflow regions characterized by
482 photochemical O₃ production from precursors (including CO) or CO destruction (both identified
483 by positive R_{O₃-CO}) from the regions characterized by O₃ loss (chemical destruction or surface
484 deposition) or by strong stratospheric contaminations (both identified by negative R_{O₃-CO}).
485 Negative R_{O₃-CO} and dO_3/dCO are measured at high latitudes of both hemispheres all over the year,
486 but more specifically at high latitudes of the S.H. in summer-fall (with R_{O₃-CO} < -0.25 on averages
487 in DJF and MMA). Given that high latitudes experience more O₃ destruction than the low latitudes
488 due to a lack of sunlight, the negative correlations for the high latitude regions might also reflect
489 air masses originating from/characterizing the stratosphere due to natural intrusion or to artificial
490 mixing with the troposphere introduced by the limited vertical sensitivity of IASI in the highest
491 latitudes (stratospheric contribution varying between ~40% and 65%; see supplementary materials
492 in Wespes et al., 2016). These processes are likely at the origin of the band-like pattern of negative
493 trends in the S.H. discussed in Sections 3 and 4.1. Negative R_{O₃-CO} and dO_3/dCO are also found
494 above the Caribbean, the Arabic Peninsula and the North Indian Ocean in JJA/SON and the South
495 Atlantic in DJF. They are in line with Kim et al. (2013) and they likely reflect the influence of
496 lightning NO_x which produce O₃ but also OH oxidizing CO (e.g. Sauvage et al., 2007; Labrador
497 et al., 2004).

498

499 Strong positive correlations are identified in both R_{O₃-CO} and dO_3/dCO patterns over the tropical
500 regions and for mid-latitudes of both Hemispheres during the peak of photochemistry in summer.
501 Maxima (R_{O₃-CO} > 0.8 and dO_3/dCO > 0.5) are detected in continental pollution outflow regions in

502 the N.H., especially downwind South-East Asia and over the South Africa/Amazonia/South
503 Atlantic region. These O₃-CO correlation patterns from IASI are fully consistent with those
504 measured by TES (Zhang et al., 2006; 2008; Voulgarakis et al., 2010) and by OMI/AIRS (Kim et
505 al., 2013), which have been interpreted with global CTM's as originating from Asian pollution
506 influence and from combustion sources including biomass burning, respectively. The high positive
507 R_{O₃-CO} found in JJA at mid-latitudes of the N.H. are detected in a lesser extent in DJF reflecting
508 the decreasing photochemistry. It is also worth pointing out in Fig. 9 the clear hemispheric
509 differences in the R_{O₃-CO} and dO₃/dCO values at mid-high latitudes and, more particularly, the shift
510 of positive R_{O₃-CO} and dO₃/dCO towards higher latitudes of the N.H. during summer (e.g. R_{O₃-CO}=
511 0.24 in summer vs 0.038 in spring in the 35°N-55°N band). As a consequence, these results suggest
512 that the band-like pattern of negative trends measured by IASI in summer might substantially
513 reflect the continental pollution influence and, hence, that it could result from the decline of
514 anthropogenic O₃ precursor emissions. Nevertheless, interpreting O₃-CO correlations in the free
515 troposphere, especially in photochemically aged pollution plumes far from the emission sources
516 towards the highest latitudes, remains complicated by the mixing of the continental combustion
517 outflow with stratospheric air masses, in addition to the background dynamic and photochemistry
518 (e.g. Liang et al., 2007).

519
520 Finally, we also provide in Fig.9c the seasonal patterns of O₃-CO covariances (COV_{O₃-CO}). They
521 confirm the band-like pattern of the weak natural variation captured in the S.H. mid-latitudes (see
522 Sections 3 and 4.1) and help identifying the region downwind East China, the northern mid-
523 latitudes outflow region and the South tropical region as the ones with the highest pollution
524 variability, in addition to the strongest O₃-CO correlations. To conclude, the particularly strong
525 positive O₃-CO relationship in terms of R_{O₃-CO}, dO₃/dCO and COV_{O₃-CO} measured over and
526 downwind North-East India/East China in summer in comparison with the ones measured
527 downwind East US and over Europe indicate that South-East Asia experiences the most of the
528 intense pollution episodes of the N.H. with the largest O₃-CO variability (COV_{O₃-CO} > 40×10³³
529 mol².cm⁻⁴) and the largest O₃ enhancement (dO₃/dCO > 0.5) over the last decade. The strong O₃-
530 CO relationship in that region is associated with the significant increase that is detected in the IASI
531 O₃ levels downwind East of Asia (see Section 4.1) despite the net decrease in O₃ precursor
532 emissions recorded in China after 2011 (e.g. Cohen et al., 2017; Miyazaki et al., 2017).

533 534 **5 Conclusions**

535
536 In this study, we have explored, for the first time, the possibility to infer significant trends in
537 tropospheric O₃ from the first ~10 years (January 2008 – May 2017) of IASI daily measurements
538 at a global scale. To this end, MLR analyses have been performed by applying a multivariate
539 regression model (annual and seasonal formulations), including a linear trend term in addition to
540 chemical and dynamical proxies, on gridded mean tropospheric ozone time series. This work
541 follows on the analysis of the main dynamical drivers of O₃ variations measured by IASI, which

542 was recently published in Wespes et al. (2017). We have first verified the performance of the MLR
543 models in explaining the variations in daily time series over the whole studied period. In particular,
544 we have shown that the model reproduces a large part of the O₃ variations (>70%) with small
545 residuals errors (*RMSE* of ~10%) at northern latitudes in summer. We have then performed O₃
546 trend sensitivity tests to verify the possibility to capture trend characteristics independently from
547 natural variations. Despite the weak contribution of trends to the total variation in the MLT O₃
548 columns at a global scale, the results demonstrate the possibility to discriminate significant trends
549 from the explanatory variables, especially in summer at mid-high latitudes of the N.H. (~45°N-
550 70°N) where the contribution and the sensitivity of trends are the largest (contribution of ~30-50%
551 and a ~10% increase in the *RMSE* excluding the LT in the model). We then focused on the
552 interpretation of the global trend estimates. We have found an interesting significant positive
553 trends in the S.H. tropical region extending from the Amazon to the tropical eastern Indian Ocean
554 and over South-East Asia in spring-summer which should however be carefully considered given
555 the high *RMSE* of the regression residuals in these regions. The MLR analysis reveals a band-like
556 pattern of high significant negative trends in the N.H. mid-high latitudes in summer (-0.47 ± 0.16
557 DU/yr on average in the 45°N-70°N band). The statistical significance of such trend estimates is
558 further verified by estimating, based on the autocorrelation and on the variance of the noise
559 residuals, the minimum number of years of IASI measurements that are required to detect a trend
560 of a $|5|$ DU/dec magnitude. The results clearly demonstrate the possibility to determine such a trend
561 amplitude from the available IASI dataset and the used MLR model at northern mid-high latitudes
562 in summer, while much larger measurement periods are necessary elsewhere. In particular, the
563 regions with the longest required period, in the tropics, highlight a series of known processes that
564 are closely related to the El-Niño dynamic, which underlies the lack of associated
565 parameterizations in the MLR model. The importance of using reliable MLR models in
566 understanding large-scale O₃ variations and in determining trends is further explored by comparing
567 the trends inferred from MLR and from SLR, the latter being still commonly used by the
568 international community. The comparison has clearly highlighted the gain of MLR in attributing
569 the trend-like segments in natural variations, such as ENSO, to the right processes and, hence, in
570 avoiding misinterpretation of “apparent” trends in the measurement datasets. Nevertheless, it is
571 worth noting that there could be a possible impact of the sampling (because of the cloud and quality
572 filters applied) and of the jump in September 2010 that has been identified in the IASI dataset (see
573 Section 2), in both MLR and SLR trends. Finally, by exploiting the simultaneous and vertically-
574 resolved O₃ and CO measurements from IASI, we have provided and used the O₃-CO correlations
575 in the troposphere to help determining the origins/characteristics of patterns of negative or positive
576 trends. The distributions have allowed us to identify, in particular, strong positive O₃-CO
577 correlations, regression slopes and covariance in the N.H. mid-latitudes and northward during
578 summer, which suggests a continental pollution influence in the N.H. band-like pattern of high
579 significant negative trends recorded by IASI and, hence, a direct effect of the policy measures
580 taken to reduce emissions of O₃ precursor species.

581

582 This study supports overall the importance of using (1) high density and long term homogenized
583 satellite records, such as those provided by IASI, and (2) complex models with predictor functions
584 that describe the O₃-regressors dependencies for a more accurate determination of trends in
585 tropospheric O₃ - as required by the scientific community, e.g. in the Intergovernmental Panel on
586 Climate Change (IPCC, 2013) - and for further resolving trend biases between independent
587 datasets (Payne et al., 2017; the TOAR report – Tropospheric Ozone Assessment Report: Present-
588 day distribution and trends of tropospheric ozone relevant to climate and global atmospheric
589 chemistry model evaluation, Lead Authors: A. Gaudel and O.R. Cooper). Determination, with
590 IASI, of robust trends in tropospheric O₃ at the global scale will be achievable in the near future
591 by merging the homogeneous O₃ profiles from the three successive instruments onboard Metop-A
592 (2006); -B (2012) and -C (2018) platforms and from the IASI-Next Generation instrument onboard
593 the Metop Second Generation series of satellites (Clerbaux and Crevoisier, 2013; Crevoisier et al.,
594 2014). A long record of tropospheric O₃ measurements will be also assured by the Cross-track
595 Infrared Sounder (CrIS) onboard the Joint Polar Satellite System series of satellites.

596

597 **Acknowledgments**

598 IASI has been developed and built under the responsibility of the Centre National d'Etudes
599 Spatiales (CNES, France). It is flown onboard the Metop satellites as part of the EUMETSAT
600 Polar System. The IASI L1 data are received through the EUMETCast near real time data
601 distribution service. We acknowledge the financial support from the ESA O₃-CCI, Copernicus O₃-
602 C3S and Eumetsat AC SAF projects. The research in Belgium is also funded by the Belgian State
603 Federal Office for Scientific, Technical and Cultural Affairs and the European Space Agency (ESA
604 Prodex IASI Flow and AC SAF).

605

606

607

608

609

610

611

612

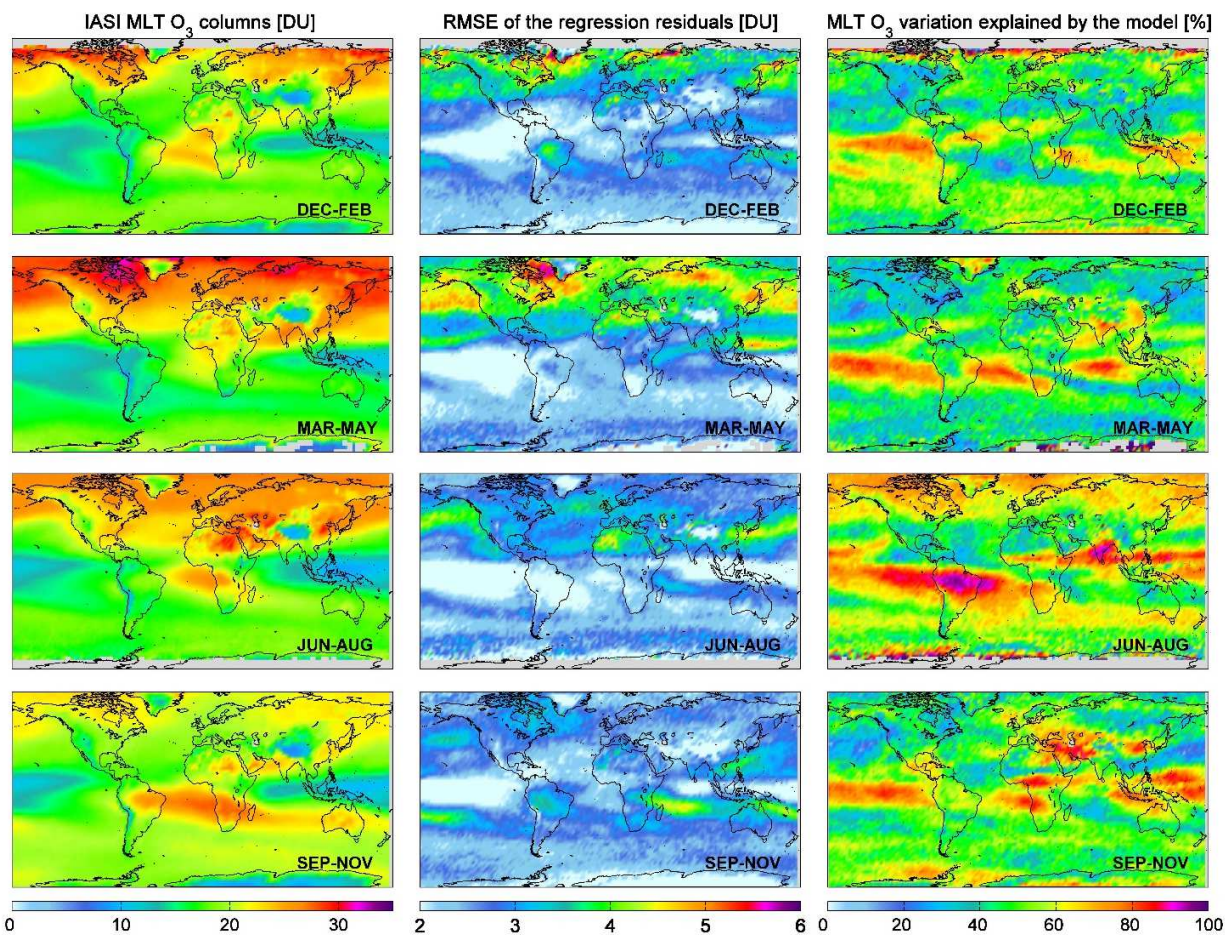
613

614

615

616 **Figure captions**

617



618

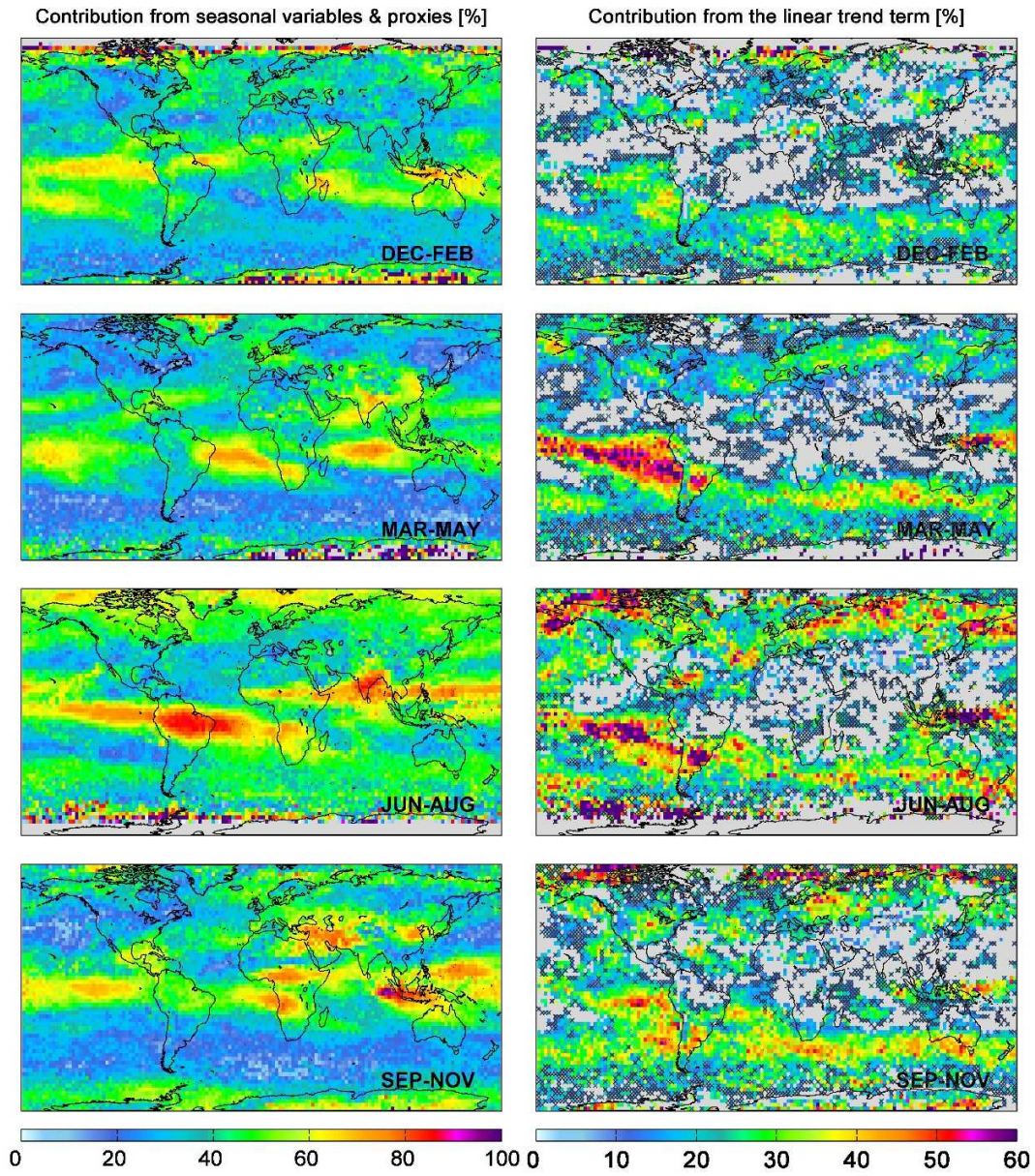
619 **Fig.1.** Seasonal distribution of O₃ tropospheric columns (in DU, integrated from ground to 300hPa)
620 measured by IASI and averaged over January 2008 – May 2017 (left panel), of the *RMSE* of the
621 regression fits (in DU, middle panel) and of the fraction of the variation in IASI data explained by
622 the regression model, calculated as $[100 \times (\sigma(O_3^{Fitted_model}(t)) / \sigma(O_3(t)))]$ (in %, right panel). Data
623 are averaged over a 2.5°x2.5° grid box.

624

625

626

627

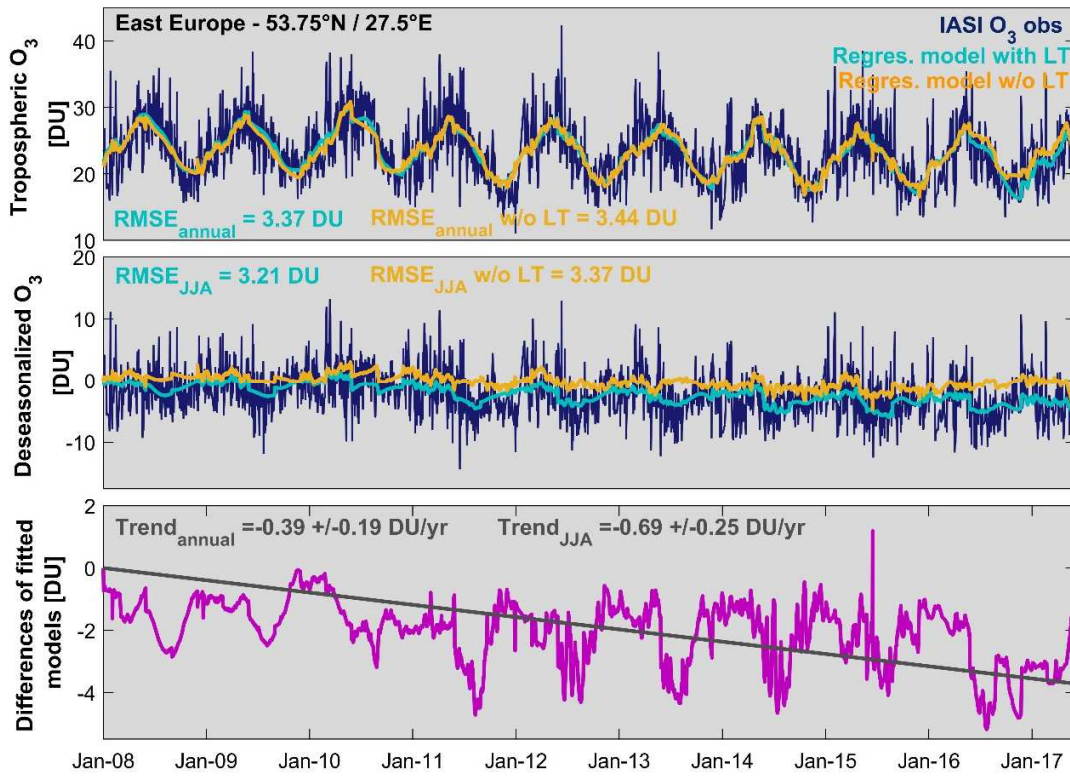


628
629
630
631
632
633
634
635
636

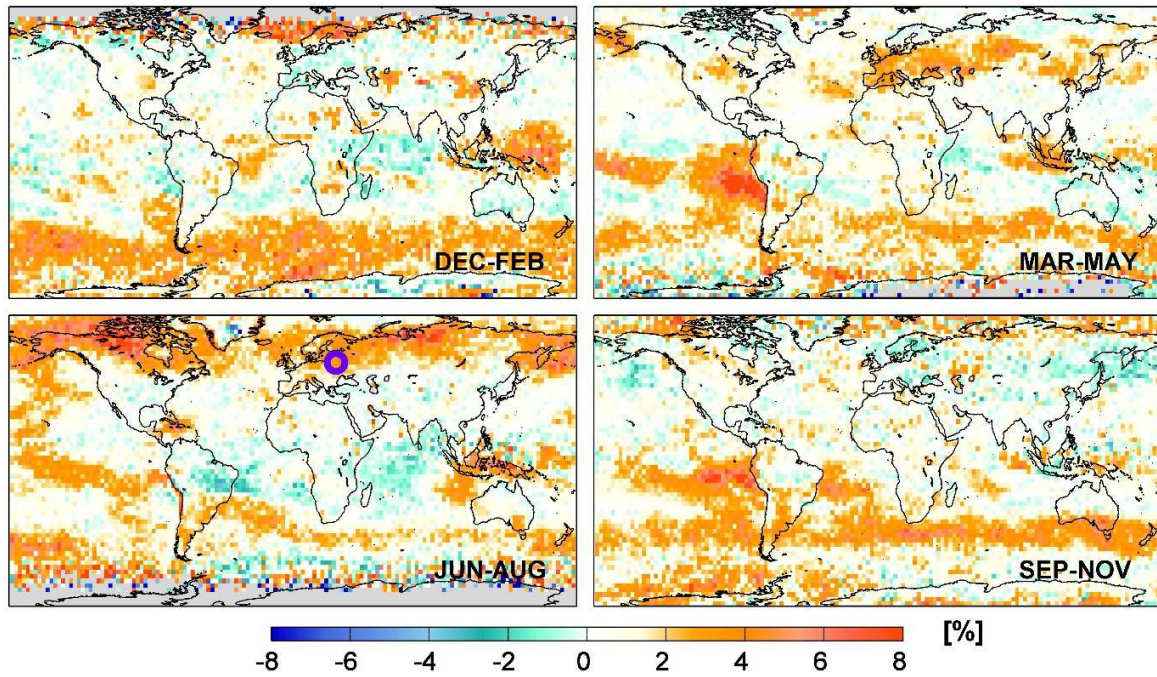
Fig.2. Seasonal distributions of the contribution from the seasonal and explanatory variables into the IASI O_3 variations estimated as

$$\left[100 \times \sigma \left(\sum_{n=1; j=2}^{4; m} [a_n; b_n; x_j [\cos(n\omega t); \sin(n\omega t); X_{norm, j}]] \right) / \sigma(O_3(t)) \right] \text{ (in \% , left panels)}$$

and of the contribution from the linear trend calculated as $[100 \times \sigma(x_{j=1} \cdot trend) / \sigma(O_3(t))]$ (in %, right panels). The grey areas and crosses refer to the non-significant grid cells in the 95% confidence limits (2σ level). Note that the scales are different.

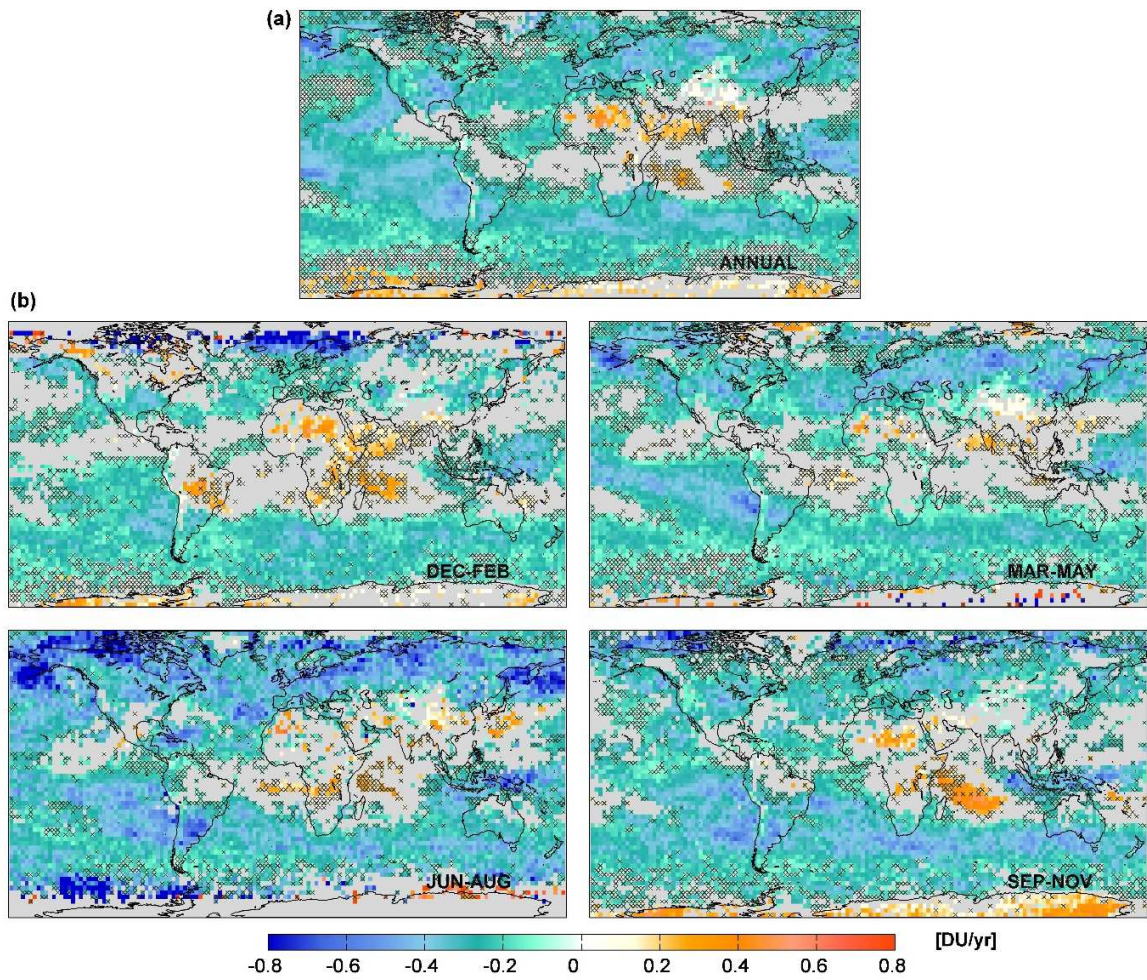


637
 638 **Fig.3.** Examples of daily time series of IASI O₃ measurements (dark blue) and of the fitted seasonal
 639 regression models with (light blue) and without (orange) the linear term in the troposphere (1st
 640 row). Daily time series of the deseasonalised O₃ (observations and regression models; 2^d row) and
 641 of the difference of the fitted models with and without the linear trend term as well as the adjusted
 642 annual trend (pink and grey lines, respectively; 3^d row) (given in DU). The *RMSE* (annual and for
 643 for the JJA period in DU) and the trend values (annual and for the JJA period in DU/yr) are also
 644 indicated.
 645
 646



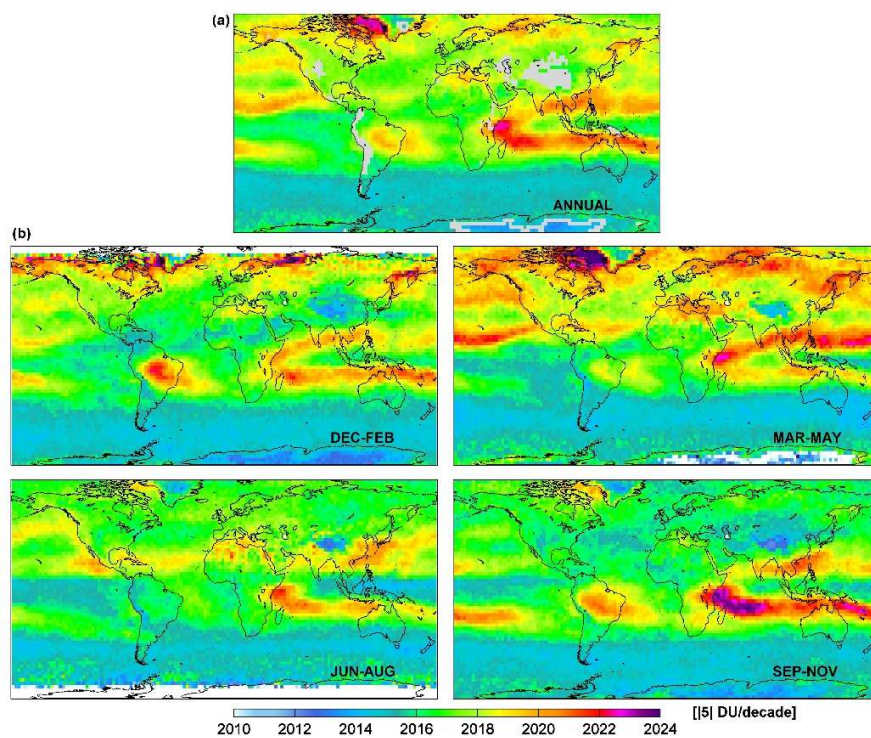
647
 648
 649
 650
 651
 652

Fig.4. Seasonal distribution of the differences between the *RMSE* of the regression fits with and without linear trend term $[(RMSE_{w/o_LT} - RMSE_{with_LT})/RMSE_{with_LT} \times 100]$ (in %). The blue circles in the JJA panel refer to the case presented in Fig.3.

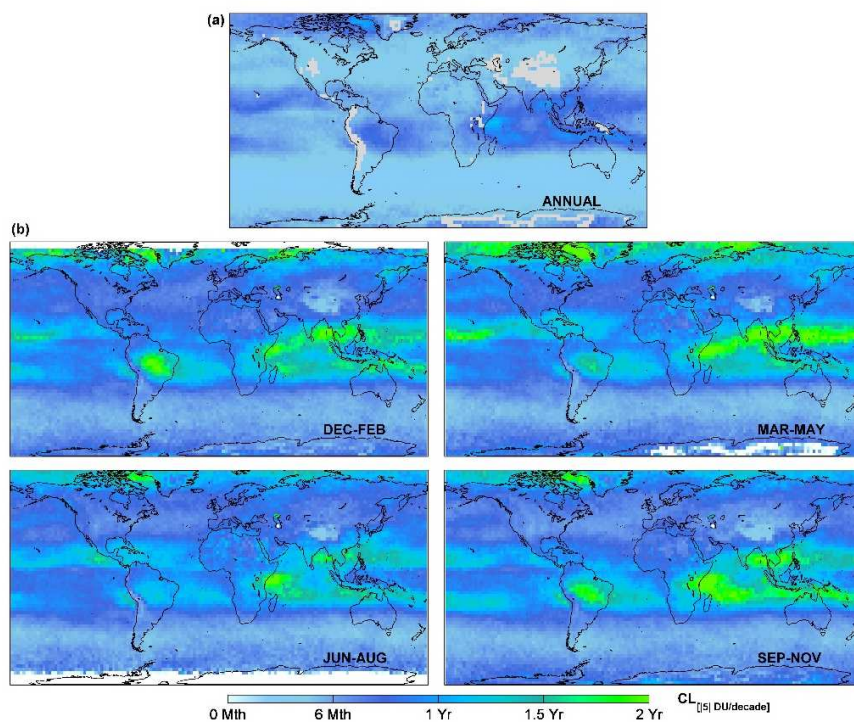


653
 654 **Fig.5.** (a) Annual and (b) seasonal distributions of the adjusted trends in DU/yr from the multi-
 655 linear regression models. The grey areas and crosses refer to the non-significant grid cells in the
 656 95% confidence limits (2σ level).

657
 658
 659

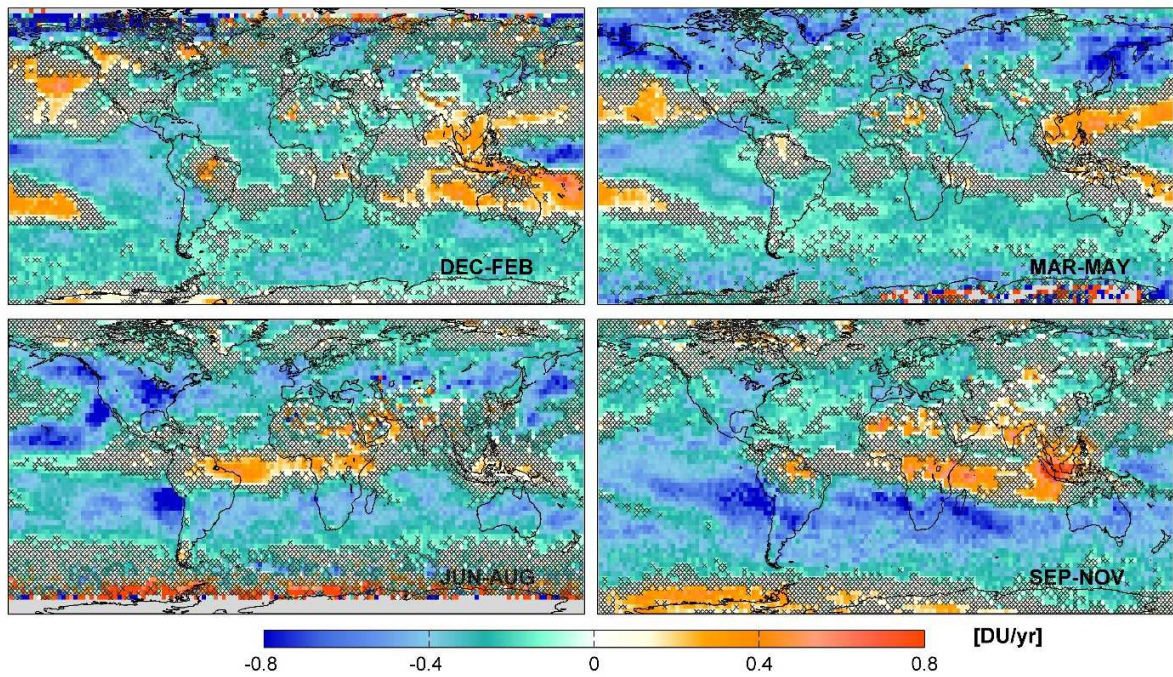


660



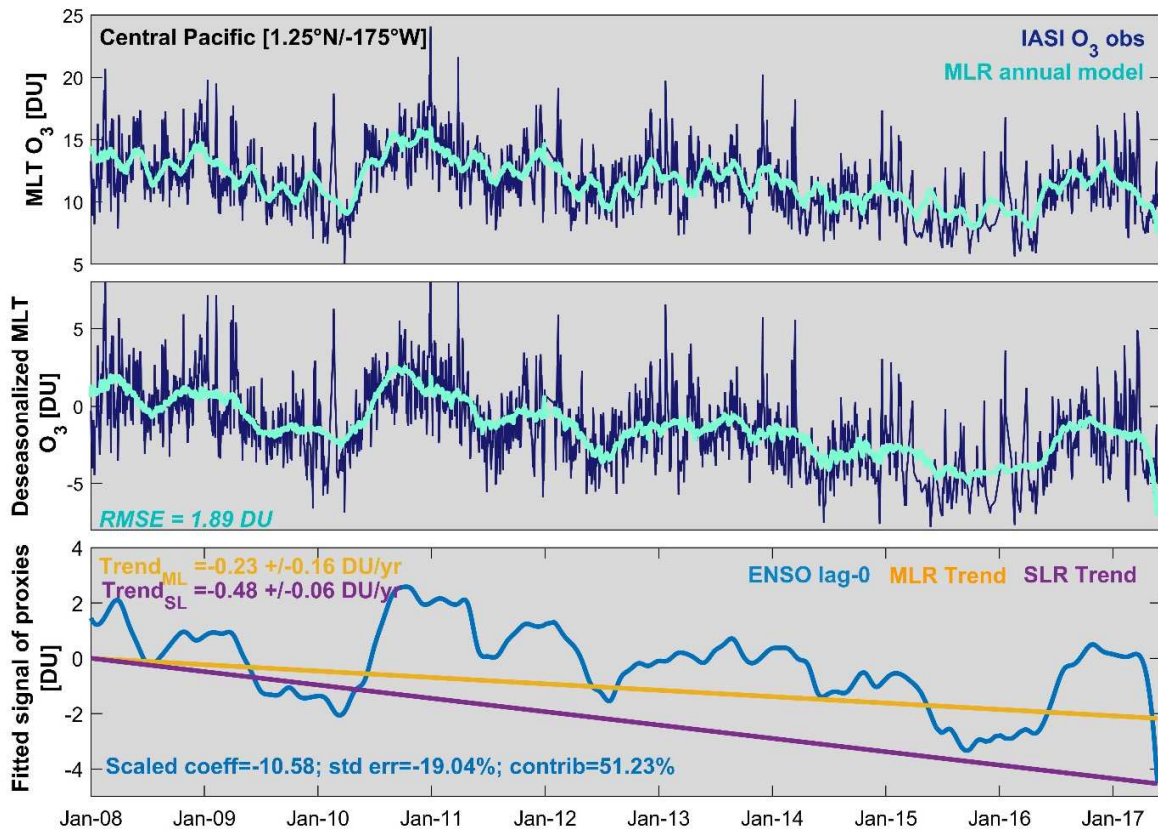
661
662
663
664
665

Fig.6 (a) Estimated year of tropospheric IASI O₃ trend detection (with a probability of 90%) for a given trend of $|5|$ DU per decade starting at the beginning of the studied period (20080101) and (b) associated maximal confidence limits from the annual (top panel) and the seasonal (bottom panels) regression models.



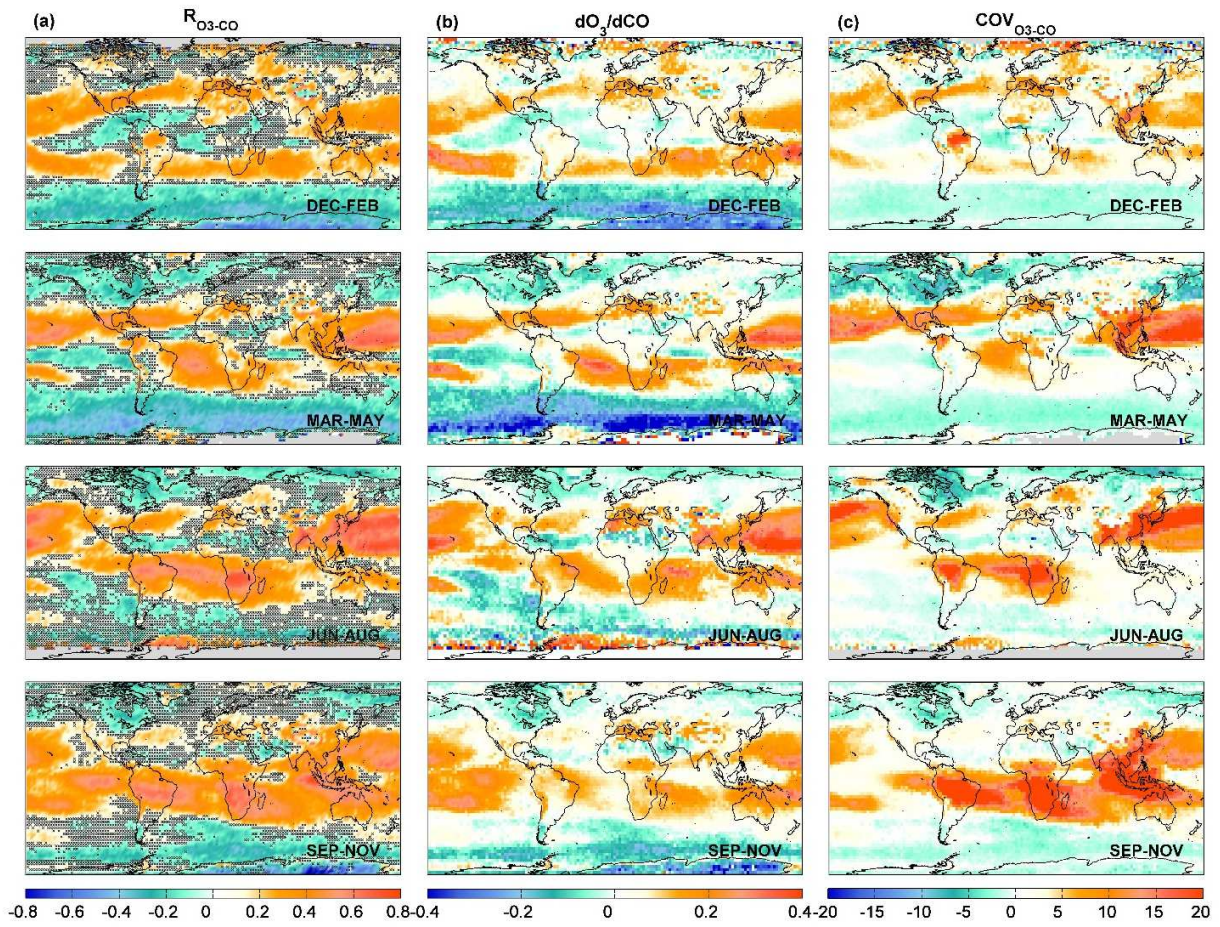
666
 667
 668
 669
 670

Fig.7. Seasonal distributions of the fitted linear term trends (given in DU/yr) derived from a single linear regression model. The crosses refer to the non-significant grid cells in the 95% confidence limits (2σ level).



671
 672 **Fig.8.** Daily time series of O₃ measured by IASI and adjusted by the multivariate annual regression
 673 model (top row and middle row for the deseasonalized O₃), along with the adjusted trends derived
 674 from the single and the multivariate linear regressions (SLR and MLR) and of the fitted signal of
 675 ENSO proxy (one of the main retained proxies in the multivariate regression model) calculated as
 676 $[x_j X_{norm,j}]$ (bottom row) over the equatorial central Pacific (negative ENSO “dynamical” effect)
 677 (given in DU). The *RMSE* of the multivariate regression fit and the fitted SLR and MLR trend
 678 values are also indicated.

679
 680
 681
 682
 683
 684



685

686 **Fig.9.** Global distributions of (a) the correlation coefficients (R_{O_3-CO}), (b) the regression slope
 687 (dO_3/dCO in $\text{mol.cm}^{-2}/\text{mol.cm}^{-2}$) and (c) the covariances (COV_{O_3-CO} in $10^{33} \text{ mol.cm}^{-2} \times \text{mol.cm}^{-2}$)
 688 of daily median IASI tropospheric O_3 and CO over January 2008 – May 2017. Data are averaged
 689 over a $2.5^\circ \times 2.5^\circ$ grid box. Crosses in R_{O_3-CO} panels (a) refer to the non-significant grid cells in the
 690 95% confidence intervals (2σ level).

691

692

693

694

695

696

697

698

699

700

701

702

703 **References**

- 704
- 705 Anton, M., D. Loyola, C. Clerbaux, M. Lopez, J. Vilaplana, M. Banon, J. Hadji-Lazaro, P. Valks,
706 N. Hao, W. Zimmer, P. Coheur, D. Hurtmans, and L. Alados-Arboledas: Validation of the Metop-
707 A total ozone data from GOME-2 and IASI using reference ground-based measurements at the
708 Iberian peninsula, *Remote Sensing of Environment*, 115, 1380-1386, 2011.
- 709
- 710 Archibald, A., Y. Elshorbany et al.: Tropospheric Ozone Assessment Report: Critical review of
711 the present-day and near future tropospheric ozone budget, *Elem. Sci. Anth.*, in-review, 2017.
- 712
- 713 Bertschi, I. T. and Jaffe, D. A.: Long-range transport of ozone, carbon monoxide, and aerosols to
714 the NE Pacific troposphere during the summer of 2003: Observations of smoke plumes from Asian
715 boreal fires, *J. Geophys. Res.*, 110(D5), D05303, doi:10.1029/2004JD005135, 2005.
- 716
- 717 Boynard, A., D. Hurtmans, M. Koukouli, et al.: Seven years of IASI ozone retrievals from FORLI:
718 validation with independent total column and vertical profile measurements, *Atmos. Meas. Tech.*,
719 9, 4327-4353, 2016.
- 720
- 721 Boynard, A., D. Hurtmans, K. Garane, F. Goutail, J. Hadji-Lazaro, M. E. Koukouli, C. Wespes,
722 A. Keppens, J.-P. Pommereau, A. Pazmino, D. Balis, D. Loyola, P. Valks, S. Hassinen, P.-F.
723 Coheur and C. Clerbaux, Validation of the IASI FORLI/Eumetsat O₃ products using satellite
724 (GOME-2), ground-based (Brewer-Dobson, SAOZ) and ozonesonde measurements, in
725 preparation for this QOS special issue.
- 726
- 727 Chen, Y., Randerson, J. T., Morton, D. C., DeFries, R. S., Collatz, G. J., Kasibhatla, P. S.,iglio,
728 L., Jin, Y., and Marlier, M. E.: Forecasting Fire Season Severity in South America Using Sea
729 Surface emperature Anomalies, *Science*, 334, 787–791, doi:10.1126/science.1209472, 2011.
- 730
- 731 Clarisse, L., Y. R'Honi ; P.-F. Coheur ; D. Hurtmans, and C. Clerbaux : Thermal infrared nadir
732 observations of 24 atmospheric gases. *Geophysical Research Letters*, 38, L10802, 2011.
- 733
- 734 Clerbaux, C., A. Boynard, L. Clarisse, M. George, J. Hadji-Lazaro, H. Herbin, D. Hurtmans, M.
735 Pommier, A. Razavi, S. Turquety, C. Wespes, and P.-F. Coheur: Monitoring of atmospheric
736 composition using the thermal infrared IASI/MetOp sounder, *Atmos. Chem. Phys.*, 9, 6041-6054,
737 2009.
- 738
- 739 Clerbaux C. and C. Crevoisier: New Directions: Infrared remote sensing of the troposphere from
740 satellite: Less, but better, *Atmospheric Environment*, 72, 24-26, 2013.
- 741
- 742 Crevoisier, C., Clerbaux, C., Guidard, V., Phulpin, T., Armante, R., Barret, B., Camy-Peyret, C.,
743 Chaboureaud, J.-P., Coheur, P.-F., Crépeau, L., Dufour, G., Labonnote, L., Lavanant, L., Hadji-
744 Lazaro, J., Herbin, H., Jacquinet-Husson, N., Payan, S., Péquignot, E., Pierangelo, C., Sellitto, P.,
745 and Stubenrauch, C. : Towards IASI-New Generation (IASI-NG): impact of improved spectral
746 resolution and radiometric noise on the retrieval of thermodynamic, chemistry and climate
747 variables, *Atmos. Meas. Tech.*, 7, 4367-4385, 2014.

748
749 Cohen, Y., et al.: Climatology and long-term evolution of ozone and carbon monoxide in the UTLS
750 at northern mid-latitudes, as seen by IAGOS from 1995-2013, ACPD, in-review, 2017.
751
752 Cooper, O., D. Parrish, A. Stohl, M. Trainer, P. Nédélec, V. Thouret, J.-P. Cammas, S. Oltmans,
753 B. Johnson and D. Tarasick: Increasing springtime ozone mixing ratios in the free troposphere
754 over western North America, *Nature*, 463, 344–348, doi:10.1038/nature08708, 2010.
755
756 Cooper, O. R., R.-S. Gao, D. Tarasick, T. Leblanc, and C. Sweeney: Long-term ozone trends at
757 rural ozone monitoring sites across the United States, 1990–2010, *J. Geophys. Res.*, 117, D22307,
758 doi:10.1029/2012JD018261, 2012.
759
760 Cooper, O. R., D. D. Parrish, J. Ziemke, N. V. Balashov, M. Cupeiro, I. E. Galbally, S. Gilge, L.
761 Horowitz, N. R. Jensen, J.-F. Lamarque, V. Naik, S. J. Oltmans, J. Schwab, D. T. Shindell, A. M.
762 Thompson, V. Thouret, Y. Wang, R. M. Zbinden: Global distribution and trends of tropospheric
763 ozone: An observation-based review, *Elementa: Science of the Anthropocene*, 2, 000029,
764 doi:10.12952/journal.elementa.000029, 2014.
765
766 Doughty, D. C., Thompson, A. M., Schoeberl, M. R., Stajner, I., Wargan, K., and Hui, W. C. J.:
767 An intercomparison of tropospheric ozone retrievals derived from two Aura instruments and
768 measurements in western North America in 2006, *J. Geophys. Res.*, 116,
769 D06303, doi:10.1029/2010JD014703, 2011.
770
771 Dufour, G., M. Eremenko, A. Griesfeller, B. Barret, E. LeFlochmoen, C. Clerbaux, J. Hadji-
772 Lazaro, P.-F. Coheur, and D. Hurtmans: Validation of three different scientific ozone products
773 retrieved from IASI spectra using ozonesondes, *Atmos. Meas. Tech.*, 5, 611-630, 2012.
774
775 Duncan, B. N., Lamsal, L. N., Thompson, A. M., Yoshida, Y., Lu, Z., Streets, D. G., Hurwitz, M.
776 M., and Pickering, K. E.: A space-based, high-resolution view of notable changes in urban
777 NO_x pollution around the world (2004-2005), *J. Geophys. Res.* 121, 976–96, 2016.
778
779 Fishman, J., K. Fakhruzzaman, B. Cros and D. Nganda: Identification of widespread pollution in
780 the southern-hemisphere deduced from satellite analyses, *Science*, 252, 1693-1696, 1991.
781
782 Fishman, J., Creilson, J. K., Wozniak, A. E., and Crutzen, P. J.: Interannual variability of
783 stratospheric and tropospheric ozone determined from satellite measurements, *J. Geophys. Res.*,
784 110, D20306, doi:10.1029/2005JD005868, 2005.
785
786 Frossard, L., H.E. Rieder, M. Ribatet, J. Staehelin, J. A. Maeder, S. Di Rocco, A. C. Davison, T.
787 Pete.: On the relationship between total ozone and atmospheric dynamics and chemistry at mid-
788 latitudes – Part 1: Statistical models and spatial fingerprints of atmospheric dynamics and
789 chemistry, *Atmos. Chem. Phys.*, 13, 147–164, doi:10.5194/acp-13-147-2013, 2013.
790

791 Fusco, A. C., and J. A. Logan: Analysis of 1970–1995 trends in tropospheric ozone at northern
792 hemisphere midlatitudes with the GEOSCHEM model, *J. Geophys. Res.*, 108(D15), 4449,
793 doi:10.1029/2002JD002742, 2003.

794

795 Gaudel, A., O. R. Cooper, G. Ancellet, B. Barret, A. Boynard, J. P. Burrows, C. Clerbaux, P.-F.
796 Coheur, J. Cuesta, E. Cuevas, S. Doniki, G. Dufour, F. Ebojie, G. Foret, O. Garcia, M. J. Granados-
797 Muñoz, J. Hannigan, F. Hase, B. Hassler, G. Huang, D. Hurtmans, D. Jaffe, N. Jones, P.
798 Kalabokas, B. Kerridge, S. Kulawik, B. Latter, T. Leblanc, E. Le Flochmoën, W. Lin, J. Liu, X.
799 Liu, E. Mahieu, A. McClure-Begley, J. Neu, M. Osman, M. Palm, H. Petetin, I. Petropavlovskikh,
800 R. Querel, N. Rahpoe, A. Rozanov, M. G. Schultz, J. Schwab, R. Siddans, D. Smale, M.
801 Steinbacher, H. Tanimoto, D. Tarasick, V. Thouret, A. M. Thompson, T. Trickl, E. Weatherhead,
802 C. Wespes, H. Worden, C. Vigouroux, X. Xu, G. Zeng, J. Ziemke: Tropospheric Ozone
803 Assessment Report: Present-day distribution and trends of tropospheric ozone relevant to climate
804 and global atmospheric chemistry model evaluation, submitted to *Elementa*.

805

806 Gazeaux, J., C. Clerbaux, M. George, J. Hadji-Lazaro, J. Kuttippurath, P.-F. Coheur, D. Hurtmans,
807 T. Deshler, M. Kovilakam, P. Campbell, V. Guidard, F. Rabier, and J.-N. Thepaut:
808 Intercomparison of polar ozone profiles by IASI/Metop sounder with 2010 concordiasi
809 ozonesonde observations, *Atmos. Meas. Tech.*, 5, 7923-7944, 2012.

810

811 Hess, P.G. and R. Zbinden: Stratospheric impact on tropospheric ozone variability and trends:
812 1990–200, *Atmos. Chem. Phys.*, 13, 649–674, 2013.

813

814 Hilton, F., R. Armante, T. August, et al. : Hyperspectral Earth Observation from IASI: Five Years
815 of Accomplishments, *Bulletin of the American Meteorological Society*, vol. 93, issue 3, pp. 347-
816 370, 2012.

817

818 Hurtmans, D., P. Coheur, C. Wespes, L. Clarisse, O. Scharf, C. Clerbaux, J. Hadji-Lazaro, M.
819 George, and S. Turquety: FORLI radiative transfer and retrieval code for IASI, *Journal of*
820 *Quantitative Spectroscopy and Radiative Transfer*, 113, 1391-1408, 2012.

821

822 Intergovernmental Panel on Climate Change, *Climate Change 2013: The Physical Science Basis.*
823 *Contribution of Working Group I to the Fifth Assessment Report of the Intergovernmental Panel*
824 *on Climate Change*, edited by T. F. Stocker et al., pp. 164–270, Cambridge Univ. Press,
825 Cambridge, U. K., and New York, 2013.

826

827 Jonson, J. E., Simpson, D., Fagerli, H., and Solberg, S.: Can we explain the trends in European
828 ozone levels?, *Atmos. Chem. phys.*, 6, 51–66, doi:10.5194/acp-6-51-2006, 2006.

829

830 Keppens, A., J.-C. Lambert, J. Granville, D. Hubert, T. Verhoelst, S. Compernelle, B. Latter, B.
831 Kerridge, R. Siddans, A. Boynard, J. Hadji-Lazaro, C. Clerbaux, C. Wespes, D. R. Hurtmans, P.-
832 F. Coheur, J. van Peet, R. van der A, K. Garane, M. E. Koukouli, D. S. Balis, A. Delcloo, R. Kivi,
833 R. Stübi, S. Godin-Beekmann, M. Van Roozendael, C. Zehner: Quality assessment of the
834 *Ozone_cci Climate Research Data Package (release 2017): 2. Ground-based validation of nadir*
835 *ozone profile data products, in preparation for this QOS special issue.*

836
837 Kim, P. S., D. J. Jacob, X. Liu, J. X. Warner, K. Yang, K. Chance, V. Thouret, and P. Nedelec:
838 Global ozone–CO correlations from OMI and AIRS: constraints on tropospheric ozone sources,
839 *Atmos. Chem. Phys.*, 13, 9321–9335, 2013.
840
841 Knibbe J. S., R. J. van der A, and A. T. J. de Laat: Spatial regression analysis on 32 years of total
842 column ozone data, *Atmos. Chem. Phys.*, 14, 8461–8482, 2014.
843
844 Krotkov, N. A., McLinden, C. A., Li, C., Lamsal, L. N., Celarier, E. A., Marchenko, S. V., Swartz,
845 W. H., Bucsela, E. J., Joiner, J., Duncan, B. N., Boersma, K. F., Veefkind, J. P., Levelt, P. F.,
846 Fioletov, V. E., Dickerson, R. R., He, H., Lu, Z., and Streets, D. G.: Aura OMI observations of
847 regional SO₂ and NO₂ pollution changes from 2005 to 2015, *Atmos. Chem. Phys.*, 16, 4605–4629,
848 doi:10.5194/acp-16-4605-2016, 2016.
849
850 Labrador, L. J., von Kuhlmann, R., and Lawrence, M. G.: Strong sensitivity of the global mean
851 OH concentration and the tropospheric oxidizing efficiency to the source of NO_x from lightning,
852 *Geophys. Res. Lett.*, 31, L06102, doi:10.1029/2003GL019229, 2004.
853
854 Lewis, S. L., Brando, P. M., Phillips, O. L., van der Heijden, G. M. F., and Nepstad, D.: The 2010
855 Amazon Drought, *Science*, 331, 554–554, doi:10.1126/science.1200807, 2011.
856
857 Liang, Q., Jaegle, L., Hudman, R. C., Turquety, S., Jacob, D. J., Avery, M. A., Browell, E. V.,
858 Sachse, G. W., Blake, D. R., Brune, W., Ren, X., Cohen, R. C., Dibb, J. E., Fried, A., Fuelberg,
859 H., Porter, M., Heikes, B. G., Huey, G., Singh, H. B., and Wennberg, P. O.: Summertime influence
860 of Asian pollution in the free troposphere over North America, *J. Geophys. Res.*, 112, D12S11,
861 doi:10.1029/2006JD007919, 2007.
862
863 Lin, M., L. W. Horowitz, O. R. Cooper, D. Tarasick, S. Conley, L. T. Iraci, B. Johnson, T. Leblanc,
864 I. Petropavlovskikh, and E. L. Yates: Revisiting the evidence of increasing springtime ozone
865 mixing ratios in the free troposphere over western North America, *Geophys. Res. Lett.*, 42, 8719–
866 8728, doi:10.1002/2015GL065311, 2015.
867
868 Liu, X., P. K. Bhartia, K. Chance, R. J. D. Spurr, and T. P. Kurosu: Ozone profile retrievals from
869 the Ozone Monitoring Instrument, *Atmos. Chem. Phys.*, 10, 2521–2537, 2010.
870
871 Liu, J., Rodriguez, J. M., Thompson, A. M., Logan, J. A., Douglass, A. R., Olsen, M. A., Steenrod,
872 S. D., and Posny, F.: Origins of tropospheric ozone interannual variation over Reunion: A model
873 investigation, *J. Geophys. Res.-Atmos.*, 121, 521–537, doi:10.1002/2015jd023981, 2016.
874
875 Liu, J., et al.: Causes of interannual variability over the southern hemispheric tropospheric ozone
876 maximum, *Atmos. Chem. Phys.*, 17, 3279–3299, 2017.
877
878 Logan, J. A., M. J. Prather, S. C. Wofsy, and M. B. McElroy: Tropospheric chemistry: A global
879 perspective, *J. Geophys. Res.*, 86 (NC8), 7210–7254, doi:10.1029/JC086iC08p07210, 1981.
880

881 Logan, J. A.: Tropospheric Ozone: Seasonal behaviour, Trends, and Anthropogenic Influence, *J.*
882 *Geophys. Res.*, 90(D6), 10 463–10 482, 1985.

883

884 Logan, J. A., and V. W. J. H. Kirchhoff: Seasonal variations of tropospheric ozone at Natal, Brazil,
885 *J. Geophys. Res.*, 91(D7), 7875–7881, doi:10.1029/JD091iD07p07875, 1986.

886

887 Logan, J. A., Staehelin, J., Megretskaia, I. A., Cammas, J.-P., Thouret, V., Claude, H., De Backer,
888 H., Steinbacher, M., Scheel, H.-E., Stübi, R., Fröhlich, M., and Derwent, R.: Changes in ozone
889 over Europe: Analysis of ozone measurements from sondes, regular aircraft (MOZAIC) and alpine
890 surface sites, *J. Geophys. Res.*, doi:10.1029/2011JD016952, 2012.

891

892 Mäder, J. A., J. Staehelin, D. Brunner, W.A. Stahel, I. Wohltmann, and T. Peter: Statistical
893 modelling of total ozone: Selection of appropriate explanatory variables, *J. Geophys. Res.*, 112,
894 D11108, doi:10.1029/2006JD007694, 2007.

895

896 Miyazaki et al.: Decadal changes in global surface NO_x emission from multi-constituent satellite
897 data assimilation, *Atmos. Chem. Phys.*, 17, 807–837, 2017.

898

899 Moxim, W. J., and H. Levy II: A model analysis of the tropical South Atlantic Ocean tropospheric
900 ozone maximum: The interaction of transport and chemistry, *J. Geophys. Res.*, 105(D13), 17393–
901 17415, doi:10.1029/2000JD900175, 2000.

902

903 Neu, J.L., T. Flury, G. L. Manney, M. L. Santee, N. J. Livesey and J. Worden, Tropospheric ozone
904 variations governed by changes in stratospheric circulation, *Nat. Geosc.*, 7, 340–344,
905 doi:10.1038/ngeo2138, 2014.

906

907 Oetjen, H., Payne, V.H., Kulawik, S.S., Eldering, A., Worden, J., Edwards, D.P., Francis, G.L.,
908 Worden, H.M., Clerbaux, C., Hadji-Lazaro, J., Hurtmans, D. : Extending the satellite data record
909 of tropospheric ozone profiles from Aura-TES to MetOp-IASI, *Atmos. Meas. Tech.*, 7, 4223-4236,
910 doi:10.5194/amt-7-4223-2014, 2014.

911

912 Oltmans, S.J, A. S. Lefohn; D. Shadwick, J. M. Harris, H.-E. Scheel, I. Galbally, D. W. Tarasick,
913 B. J. Johnson, E.G. Brunke, H. Claude, G. Zeng, S. Nichol, F.J. Schmidlin, J. Davies, E. Cuevas,
914 A. Redondas, H. Naoe, T. Nakano, T. Kawasato: Recent Tropospheric Ozone Changes - A Pattern
915 Dominated by Slow or No Growth, *Atmospheric Environment*, 67, p. 331-351,
916 10.1016/j.atmosenv.2012.10.057, 2013.

917

918 Oman, L. D., Douglass, A. R., Ziemke, J. R., Rodriguez, J. M., Waugh, D. W., and Nielsen, J. E.:
919 The ozone response to ENSO in Aura satellite measurements and a chemistry–climate simulation,
920 *J. Geophys. Res.-Atmos.*, 118, 965–976, 2013.

921

922 Parrington, M., P. I. Palmer, D. K. Henze, D. W. Tarasick, E. J. Hyer, R. C. Owen, D. Helmig, C.
923 Clerbaux, K. W. Bowman, M. N. Deeter, E. M. Barratt, P.-F. Coheur, D. Hurtmans, Z. Jiang, M.
924 George, and J. R. Worden: The influence of boreal biomass burning emissions on the distribution

925 of tropospheric ozone over north America and the north Atlantic during 2010, *Atmos. Chem.*
926 *Phys.*, 12, 2077-2098, doi: 10.5194/acp-12-2077-2012, 2012.
927

928 Parrish, D.D., Holloway, J.S., Trainer, M., Murphy, P.C., Forbes, G.L., and Fehsenfeld, F.C.:
929 Export of North American Ozone Pollution to the North Atlantic Ocean, *Science*, 259, 1436–1439,
930 1993.
931

932 Parrish, D.D., K.S. Law, J. Staehelin, R. Derwent, O.R. Cooper, et al.: Long-term changes in lower
933 tropospheric baseline ozone concentrations at northern mid-latitudes. *Atmos. Chem. Phys.* 12:
934 11485–11504. doi:10.5194/acp-12-11485-2012, 2012.
935

936 Payne, V. H., J. L. Neu and H. M. Worden: Satellite observations for understanding the drivers of
937 variability and trends in tropospheric ozone, *J. Geophys. Res.*, in-press, 2017.
938

939 Pommier, M., C. Clerbaux, K. S. Law, G. Ancellet, P. Bernath, P.-F. Coheur, J. Hadji- Lazaro, D.
940 Hurtmans, P. Nedelec, J.-D. Paris, F. Ravetta, T. B. Ryerson, H. Schlager, and A. J. Weinheimer:
941 Analysis of IASI tropospheric O₃ data over the arctic during POLARCAT campaigns in 2008,
942 *Atmos. Chem. Phys.*, 12, 7371-7389, doi:doi:10.5194/acp-12-7371-2012, 2012.
943

944 Rieder, H. E., Frossard, L., Ribatet, M., Staehelin, J., Maeder, J. A., Di Rocco, S., Davison, A. C.,
945 Peter, T., Weihs, P., and Holawe, F.: On the relationship between total ozone and atmospheric
946 dynamics and chemistry at mid-latitudes – Part 2: The effects of the El Nino/Southern Oscillation,
947 volcanic eruptions and contributions of atmospheric dynamics and chemistry to long-term total
948 ozone changes, *Atmos. Chem. Phys.*, 13, 165–179, 2013.
949

950 Rodgers, C. D.: *Inverse Methods for Atmospheric Sounding: Theory and Practice*, World
951 Scientific, Series on Atmospheric, Oceanic and Planetary Physics, 2, Hackensack, N. J., 2000.
952

953 Safieddine, S., Boynard, A., Coheur, P.-F., Hurtmans, D., Pfister, G., Quennehen, B., Thomas, J.
954 L., Raut, J.-C., Law, K. S., Klimont, Z., Hadji-Lazaro, J., George, M., and Clerbaux, C.:
955 Summertime tropospheric ozone assessment over the Mediterranean region using the thermal
956 infrared IASI/MetOp sounder and the WRF-Chem model, *Atmos. Chem. Phys.*, 14, 10119–10131,
957 doi:10.5194/acp-14-10119-2014, 2014.
958

959 Saunio, M., Emmons, L., Lamarque, J.-F., Tilmes, S., Wespes, C., Thouret, V., and Schultz, M.:
960 Impact of sampling frequency in the analysis of tropospheric ozone observations, *Atmos. Chem.*
961 *Phys.*, 12, 6757–6773, doi:10.5194/acp-12-6757-2012, 2012.
962

963 Sauvage, B., Thouret, V., Thompson, A. M., Witte, J. C., Cammas, J. P., Nedelec, P., and Athier,
964 G.: Enhanced view of the “tropical Atlantic ozone paradox” and “zonal wave one” from the in situ
965 MOZAIC and SHADOZ data, *J. Geophys. Res.-Atmos.*, 111, D01301,
966 doi:10.1029/2005jd006241, 2006.
967

968 Sauvage, B., Martin, R. V., van Donkelaar, A., and Ziemke, J. R.: Quantification of the factors
969 controlling tropical tropospheric ozone and the South Atlantic maximum, *J. Geophys. Res.-*
970 *Atmos.*, 112, D11309, doi:10.1029/2006jd008008, 2007.

971

972 Scannell, C., D. Hurtmans, A. Boynard, J. Hadji-Lazaro, M. George, A. Delcloo, A. Tuinder, P.F.
973 Coheur, and C. Clerbaux: Antarctic ozone hole as observed by IASI/MetOp for 2008-2010, *Atmos.*
974 *Meas. Tech.*, 5, 123-139, 2012.

975

976 Simon, H., A. Reff, B. Wells, J. Xing, and N. Frank: Ozone Trends Across the United States over
977 a Period of Decreasing NO_x and VOC Emissions, *Environ. Sci. Technol.*, 49, 186–195,
978 dx.doi.org/10.1021/es504514z, 2015.

979

980 Stohl, A., S. Eckhardt, C. Forster, P. James, and N. Spichtinger: On the pathways and timescales
981 of intercontinental air pollution transport. *J. Geophys. Res.* 107 (D23), 4684,
982 doi:10.1029/2001JD001396, 2002.

983

984 Thompson, D. W. J. and J.M. Wallace: Annular modes in the extratropical circulation. Part I:
985 month-to month variability, *J. Climate*, 13, 1000–1016, 2000.

986

987 Thompson, A.M., J.C. Witte, H.G.J. Smit, S.J. Oltmans, B.J. Johnson, V.W.J H. Kirchhoff, and
988 F.J. Schmidlin: Southern Hemisphere Additional Ozonesondes (SHADOZ) 1998-2004 tropical
989 ozone climatology: 3. Instrumentation, station-to-station variability, and evaluation with simulated
990 flight profiles, *J. Geophys. Res.*, 112, D03304, doi:10.1029/2005JD007042, 2007.

991

992 Tarasick et al.: Tropospheric Ozone Assessment Report: Tropospheric ozone observations, *Elem.*
993 *Sci. Anth.*, in-review, 2017.

994

995 Thouret, V., J.-P. Cammas, B. Sauvage, G. Athier, R. Zbinden, R., P. Nédélec, P. Simon, and F.
996 Karcher: Tropopause referenced ozone climatology and inter-annual variability (1994–2003) from
997 the MOZAIC programme, *Atmos. Chem. Phys.*, 6, 1033–1051, doi:10.5194/acp-6-1033-2006,
998 2006.

999

1000 Tiao, G. C., G. C. Reinsel, D. Xu, J. H. Pedrick, X. Zhu, A. J. Miller, J. J. DeLuisi, C. L. Mateer,
1001 and D. J. Wuebbles, Effects of autocorrelation and temporal sampling schemes on estimates of
1002 trend and spatial correlation, *J. GeophysR. es.*, 95, 20,507-20,517, 1990.

1003

1004 Tocquer, F., Barret, B., Mari, C., Le Flochmoen, E., Cammas, J. P., and Sauvage, B.: An upper
1005 tropospheric 'ozone river' from Africa to India during the 2008 Asian post-monsoon season, *Tellus*
1006 *B*, 67, 25350, doi:10.3402/tellusb.v67.25350, 2015.

1007

1008 Valks, P., N. Hao, S. Gimeno Garcia, D. Loyola, M. Dameris, P. Jöckel, and A. Delcloo: Tropical
1009 tropospheric ozone column retrieval for GOME-2, *Atmos. Meas. Tech.*, 7, 2513–2530,
1010 doi:10.5194/amt-7-2513-2014, 2014.

1011

1012 Van der A, R. J., et al.: Cleaning up the air: effectiveness of air quality policy for SO₂ and NO_x
1013 emissions in China, *Atmos. Chem. Phys.*, 17, 1775–1789, 2017.
1014

1015 Verstraeten, W.W., J.L. Neu, J.E. Williams, K.W. Bowman, J.R. Worden and K.F. Boersma:
1016 Rapid increases in tropospheric ozone production and export from China, *Nature Geosciences*,
1017 doi: 10.1038/NGEO2493, 2015.
1018

1019 Voulgarakis, A., Telford, P. J., Aghedo, A. M., Braesicke, P., Faluvegi, G., Abraham, N. L.,
1020 Bowman, K. W., Pyle, J. A., and Shindell, D. T.: Global multi-year O₃-CO correlation patterns
1021 from models and TES satellite observations, *Atmos. Chem. Phys.*, 11, 5819–5838,
1022 doi:10.5194/acp-10-2491-2010, 2010.
1023

1024 Voulgarakis, A., P. Hadjinicolaou, J. A. Pyle: Increases in global tropospheric ozone following an
1025 El Nino event: examining stratospheric ozone variability as a potential driver, *Atmos. Sci. Let.* 12:
1026 228–232, doi: 10.1002/asl.318, 2011.
1027

1028 Weatherhead, E.C., G. C. Reinsel, G. C. Tiao, X.-L. Meng, D. Choi, W.-K. Cheang, T. Keller, J.
1029 DeLuisi, D. J. Wuebbles, J. B. Kerr, A. J. Miller, S. J. Oltmans and J. E. Frederick: Factors
1030 affecting the detection of trends: Statistical considerations and applications to environmental data,
1031 *J. Geophys. Res. Atmos.*, 103, 17149–17161, 1998.
1032

1033 Wespes, C., D. Hurtmans, L.K. Emmons, S. Safieddine, C. Clerbaux, D.P. Edwards, and P.-F.
1034 Coheur: Ozone variability in the troposphere and the stratosphere from the first six years of IASI
1035 observations (2008-2013), *Atmos. Chem. Phys.*, 16, 5721-5743, 2016.
1036

1037 Wespes, C., D. Hurtmans, C. Clerbaux, and P.-F. Coheur: O₃ variability in the troposphere as
1038 observed by IASI over 2008–2016 — Contribution of atmospheric chemistry and dynamics, *J.*
1039 *Geophys. Res. Atmos.*, 122, 2429–2451, doi:10.1002/2016JD025875, 2017.
1040

1041 Wilson, R. C., Z.L. Fleming, P.S. Monks, G. Clain, S.Henne, I.B. Konovalov, S. Szopa, and L.
1042 Menut: Have primary emission reduction measures reduced ozone across Europe? An analysis of
1043 European rural background ozone trends 1996–2005, *Atmos. Chem. Phys.*, 12, 437–454,
1044 doi:10.5194/acp-12-437-2012, 2012.
1045

1046 Worden, J., Jiang, Z., Jones, D.B.A., Alvarado, M., Bowman, K., Frankenberg, C., Kort, E.A.,
1047 Kulawik, S., S., Lee, M., Liu, J., Payne, V., Wecht, K., Worden, H.: El Niño, the 2006 Indonesian
1048 peat fires, and the distribution of atmospheric methane, *Geophys. Res. Let.*, V40, 1–6,
1049 doi:10.1002/grl.50937, 2013.
1050

1051 Zbinden, R. M., J.-P. Cammas, V. Thouret, P. Nédélec, F. Karcher, and P. Simon: Mid-latitude
1052 tropospheric ozone columns from the MOZAIC program: climatology and interannual variability,
1053 *Atmos. Chem. Phys.*, 6, 1053–1073, doi:10.5194/acp-6-1053-2006, 2006.
1054
1055

1056 Zeng, G., Morgenstern, O., Shiona, H., Thomas, A. J., Querel, R. R., and Nichol, S. E.: Attribution
1057 of recent ozone changes in the Southern Hemisphere mid-latitudes using statistical analysis and
1058 chemistry-climate model simulations, *Atmos. Chem. Phys.* 17, 10495-10513, 2017.
1059

1060 Zhang, L., Jacob, D. J., Bowman, K. W., Logan, J. A., Turquety, S., Hudman, R. C., Li, Q., Beer,
1061 R., Worden, H. M., Worden, J. R., Rinsland, C. P., Kulawik, S. S., Lampel, M. C., Shephard, M.
1062 W., Fisher, B. M., Eldering, A., and Avery, M. A.: Ozone-CO correlations determined by the TES
1063 satellite instrument in continental outflow regions, *Geophys. Res. Lett.*, 33, L18804,
1064 doi:10.1029/2006GL026399, 2006.
1065

1066 Zhang, L., Jacob, D. J., Boersma, K. F., Jaffe, D. A., Olson, J. R., Bowman, K. W., Worden, J. R.,
1067 Thompson, A. M., Avery, M. A., Cohen, R. C., Dibb, J. E., Flock, F. M., Fuelberg, H. E., Huey,
1068 L. G., McMillan, W. W., Singh, H. B., and Weinheimer, A. J.: Transpacific transport of ozone
1069 pollution and the effect of recent Asian emission increases on air quality in North America: an
1070 integrated analysis using satellite, aircraft, ozonesonde, and surface observations, *Atmos. Chem.*
1071 *Phys.*, 8, 6117–6136, doi:10.5194/acp-8-6117-2008, 2008.
1072

1073 Zhang, L., Li, Q. B., Murray, L. T., Luo, M., Liu, H. and co-authors: A tropospheric ozone
1074 maximum over the equatorial Southern Indian Ocean. *Atmos. Chem. Phys.* 12, 4279-4296, 2012.
1075

1076 Zhang, Y., O. R. Cooper, A. Gaudel, A. M. Thompson, P. Nédélec, S.-Y. Ogino and J. J. West
1077 (2016), Tropospheric ozone change from 1980 to 2010 dominated by equatorward redistribution
1078 of emissions, *Nature Geoscience*, doi: 10.1038/NGEO2827, 2016.
1079

1080 Zhao, B., Wang, S. X., Liu, H., Xu, J. Y., Fu, K., Klimont, Z., Hao, J. M., He, K. B., Cofala, J.,
1081 and Amann, M.: NO_x emissions in China: historical trends and future perspectives, *Atmos. Chem.*
1082 *Phys.*, 13, 9869-9897, doi:10.5194/acp-13-9869-2013, 2013.
1083

1084 Ziemke, J. R., A.R. Douglass, L.D. Oman, S.E. Strahan, and B.N. Duncan: Tropospheric ozone
1085 variability in the tropics from ENSO to MJO and shorter timescales, *Atmos. Chem. Phys.*, 15,
1086 8037–8049, 2015.